



HAL
open science

Microtubule Dynamics Scale with Cell Size to Set Spindle Length and Assembly Timing

Benjamin Lacroix, Gaelle Letort, Laras Pitayu, Jeremy Sallé, Marine Stefanutti, Gilliane Maton, Anne-Marie Ladouceur, Julie C Canman, Paul S Maddox, Amy S Maddox, et al.

► **To cite this version:**

Benjamin Lacroix, Gaelle Letort, Laras Pitayu, Jeremy Sallé, Marine Stefanutti, et al.. Microtubule Dynamics Scale with Cell Size to Set Spindle Length and Assembly Timing. *Developmental Cell*, 2018, 45 (4), pp.496-511.e6. 10.1016/j.devcel.2018.04.022 . hal-01864170v1

HAL Id: hal-01864170

<https://hal.science/hal-01864170v1>

Submitted on 29 Aug 2018 (v1), last revised 31 Aug 2018 (v2)

HAL is a multi-disciplinary open access archive for the deposit and dissemination of scientific research documents, whether they are published or not. The documents may come from teaching and research institutions in France or abroad, or from public or private research centers.

L'archive ouverte pluridisciplinaire **HAL**, est destinée au dépôt et à la diffusion de documents scientifiques de niveau recherche, publiés ou non, émanant des établissements d'enseignement et de recherche français ou étrangers, des laboratoires publics ou privés.

Microtubule Dynamics Scale with Cell Size to Set Spindle Length and Assembly Timing

Authors:

Benjamin Lacroix^{1*}, Gaëlle Letort², Laras Pitayu¹, Jérémy Sallé¹, Marine Stefanutti¹, Gilliane Maton¹, Anne-Marie Ladouceur³, Julie C. Canman⁴, Paul S. Maddox³, Amy S. Maddox³, Nicolas Minc¹, François Nédélec^{5*} & Julien Dumont^{1,6*}

Affiliations:

¹Institut Jacques Monod, CNRS, UMR 7592, University Paris Diderot, Sorbonne Paris Cité, F-75205, Paris, France.

²Institut Curie, Mines Paris Tech, Inserm, U900, PSL Research University, F-75005, Paris, France.

³Department of Biology, University of North Carolina, Chapel Hill, NC 27599, USA.

⁴Columbia University Medical Center, Department of Pathology and Cell Biology, New York, NY 10032, USA.

⁵Cell Biology and Biophysics Unit, European Molecular Biology Laboratory, 69117 Heidelberg, Germany.

⁶Lead contact

*Correspondence: julien.dumont@ijm.fr or benjamin.lacroix@ijm.fr or nedelec@embl.de

Summary

Successive cell divisions during embryonic cleavage create increasingly smaller cells, so intracellular structures must adapt their size to remain functional. Mitotic spindle size correlates with cell size, but the mechanisms for this scaling remain unclear. Using live cell imaging, we analyzed spindle scaling during embryo cleavage in the nematode *Caenorhabditis elegans* and sea urchin *Paracentrotus lividus*. We reveal a conserved scaling mechanism, where the growth rate of spindle microtubules scales with cell volume, which explains spindle shortening. Spindle assembly timing is however constant throughout successive divisions. Analyses *in silico* suggest that controlling the microtubule growth rate is sufficient to scale spindle length and maintain a constant assembly timing. We tested our *in silico* predictions to demonstrate that modulating cell volume or microtubule growth rate *in vivo* induces a proportional spindle size change. Our results suggest that scalability of the microtubule growth rate when cell size varies could prevent embryonic aneuploidy.

Keywords:

Microtubules, microtubule dynamics, mitotic spindle, spindle assembly, intracellular scaling, cell division, chromosome segregation, embryonic development, *in silico* models, *Caenorhabditis elegans*, *Paracentrotus lividus*.

Introduction

Eukaryotic cells range in size over six orders of magnitude. Regardless of size from the smallest unicellular eukaryote *Ostreococcus tauri* (<1 μm) to long motor neurons (>1 m long), all cells contain a common set of organelles and subcellular structures. This requirement mandates a strict scaling between these intracellular components and cell size. One striking example of this scaling is the progressive decrease in cell volume that occurs during cleavage of early embryos. Early embryonic development usually occurs without an increase in the overall embryo volume. Each round of cell division yields half the size of blastomeres, so blastomere volume can decrease by two orders of magnitude from single celled-zygotes to multicellular gastrulae (O'Farrell et al., 2004). Thus, intracellular structures and organelles must adapt to this wide range of cell dimensions by adjusting their spatial distribution and/or size to remain functional (West and Brown, 2005). Organelles known to exhibit size adaptation to cell volume variations include nuclei, cilia, endoplasmic reticulum, and cytoskeletal assemblies like the metaphase spindle (reviewed in (Chan and Marshall, 2010, 2012; Levy and Heald, 2012; Marshall, 2015b; Reber and Goehring, 2015).

The metaphase spindle is a bipolar structure composed of highly dynamic microtubules. Adapting spindle length to cell volume enables accurate chromosome segregation and spindle orientation to accommodate different scales (Dumont and Mitchison, 2009a; Holmfeldt et al., 2006; Lancaster et al., 2013). Spindle length scaling among different organisms can occur through biochemical variations in cytoplasmic content. For example, a single amino-acid change in the microtubule-severing protein katanin primarily accounts for the spindle length difference observed between oocytes from *Xenopus laevis* and the smaller closely related frog *Xenopus tropicalis* (Brown et al., 2007; Loughlin et al., 2011). In contrast, the biochemical composition of

different sized blastomeres from a given species is assumed to be constant (Mitchison et al., 2015). During cleavage of the large *X. laevis* embryo, spindle length remains constant for the first five divisions and then decreases linearly with blastomere radius for the next 5-7 divisions (Wuhr et al., 2008). In contrast, the smaller *C. elegans* embryo shows spindle length proportional to cell length from the first division throughout cleavage (Decker et al., 2011; Hara and Kimura, 2009, 2013). Seminal experiments using artificially encapsulated extracts from *X. laevis* oocytes or embryos demonstrated that spindle length directly corresponds to the size of the encapsulating droplet (Good et al., 2013; Hazel et al., 2013). These experiments accurately recapitulated the spindle scaling observed in intact embryos with a linear relationship between spindle length and droplet radius in small droplets and an upper limit to spindle length in large droplets. Intrinsic spindle mechanisms, such as balancing force between opposed motors, may account for the upper limit of spindle length scaling (Dumont and Mitchison, 2009a, b; Reber and Goehring, 2015). In contrast, extrinsic spindle mechanisms, such as component limitation, have been proposed to explain how different cytoplasm volumes with a given composition may produce different spindle lengths (Goehring and Hyman, 2012; Marshall, 2015a; Mitchison et al., 2015; Reber and Goehring, 2015; Reber and Hyman, 2015). In *C. elegans* early embryos, decreasing spindle length correlates with a progressive reduction in the amount of centrosomal components and with a decaying gradient of the microtubule-associated protein TPXL-1 (ortholog of TPX2) along spindle microtubules (Greenan et al., 2010). Experiments performed in *Xenopus* egg or embryo extracts, suggest that titration of tubulin heterodimers, limited amount/activity of the microtubule polymerase XMAP215 or cortical sequestration of Importin α , the negative regulator of the microtubule depolymerase KIF2A, could participate in spindle length scaling

(Reber et al., 2013; Wilbur and Heald, 2013). Our understanding of how the limited amount of these factors controls spindle size is in the initial stages.

The limited supply or local inactivation of key factor(s) could directly regulate spindle microtubule dynamics to efficiently control spindle length (Andersen, 2000; Andersen et al., 1997; Desai and Mitchison, 1997; Goshima et al., 2005b; Picone et al., 2010; Tournebize et al., 2000; Verde et al., 1992). Both *in vitro* and *in vivo*, microtubules alternate between phases of growth and shrinkage in a process called dynamic instability (Mitchison and Kirschner, 1984). Four parameters define these dynamic properties of microtubules, their velocities of growth and shrinkage and their frequencies of transitions between these two states called catastrophe and rescue (Kirschner and Mitchison, 1986; Walker et al., 1988). Typically, long interphasic microtubules display low catastrophe and high rescue frequencies (Belmont et al., 1990; Verde et al., 1992; Verde et al., 1990). Microtubules in this state are “unbounded” and continuously elongate over time. In contrast, microtubules shorten upon mitotic entry, due to a sharp increase in catastrophe frequency and a significant decrease in rescue events. In this regime or “bounded” state, microtubules tend to disassemble, where their average growth velocity, termed J , is negative. A steady population of microtubules can only be maintained, because a finite fraction is continuously nucleated and polymerized *de novo* (Mitchison et al., 2015; Verde et al., 1992). This regime establishes a distribution of microtubule lengths to dictate a steady state spindle size. So, precise control of microtubule dynamics during mitosis in cleaving embryos becomes an attractive candidate to adjust spindle length for blastomere size. However, the functional link between microtubule dynamics and spindle length scaling as a function of cell volume during embryo cleavage remains unknown.

Results

Microtubule Dynamics are Modulated During C. elegans Embryo Cleavage

We first determined the potential relationship among metaphase spindle length, cell volume and microtubule dynamics from the 1- to the 16-cell stage in cleaving *C. elegans* embryos. We combined high-temporal single plane confocal microscopy and 2-photon 3D-volumetric reconstructions of live embryos expressing GFP-tagged microtubules or a plasma membrane marker respectively (Figure 1A and S1A,B). In line with previous studies, we found that spindle length and cell volume progressively decreased across early embryogenesis in *C. elegans* (Figure S1C-F) (Decker et al., 2011; Greenan et al., 2010; Hara and Kimura, 2009, 2013). To determine if microtubule dynamics vary concomitantly with spindle length and cell volume, we generated kymographs of individual microtubules from our high frame-rate, single-plane confocal series of embryos expressing GFP-tagged β -tubulin (Figure 1B). This approach allowed us to identify phases of elongation and shortening and to measure the rate and duration for each phase. We observed that microtubule growth rates and durations were significantly higher for astral microtubules than spindle microtubules in all blastomeres from the 1- to the 16-cell stage, in agreement with published results for the 1-cell stage (Figure 1C (Srayko et al., 2005)). In addition, we found that microtubule dynamics parameters for both types of microtubules varied throughout development. While we found a notable, but mild decrease in the shrinkage duration between the 1- and the 16-cell stage, the most striking variation across divisions was the continuous and significant decrease in microtubule growth rate for both astral and spindle microtubules (Figure 1C). Importantly, we obtained similar rates and frequencies using a different promoter to drive expression of our GFP-tagged β -tubulin reporter or mCherry-tagged β -tubulin (Figure S2A,C and Table S1). These results suggest that microtubule dynamics

vary throughout early embryonic divisions, with a distinct decrease in the microtubule growth rate associated with decreased blastomere volume.

To investigate a potential link between these variations in microtubule dynamics and spindle length, we first determined if the length of metaphase spindles reached a steady state or if it was limited by the duration of the cell cycle and the time available before anaphase onset. Indeed, cell divisions in cleaving embryos of most species are particularly rapid, and spindle length increases continuously from nuclear envelope breakdown (NEBD) to anaphase onset (Mitchison et al., 2015). However, delaying anaphase onset in *C. elegans* embryos using a proteasome inhibitor did not induce spindle elongation above the normal metaphase spindle length at any analyzed stage (Figure S3) (Labbe et al., 2004). Moreover, the measured microtubule dynamics parameters indicate that all microtubules are in the “bounded” regime ($J < 0$) at every stage of embryo cleavage, which is compatible with a steady state (Figure S2B and Table S1A,C) (Verde et al., 1992). These results suggest that mitotic spindles in early *C. elegans* embryos reach a steady state length before anaphase onset that is not dependent on the duration needed for spindle assembly. Overall, our results demonstrate that microtubule dynamic instability evolves during embryo cleavage with the microtubule growth rate continuously decreasing in parallel with the progressive reduction of steady state spindle length.

Spindle Microtubule Growth Rate Adapts to Cell Volume in C. elegans

We next asked if variations in microtubule dynamics parameters during early embryogenesis were either a direct consequence of cell size changes or under the control of a developmental program. So, we analyzed the direct correlation between cell volume and microtubule dynamics parameters (Figure 2A,B). This analysis revealed that the growth rate of spindle microtubules most significantly correlated with cell volume (Figure 2B). So, we tested if

the decrease in cell volume of dividing blastomeres solely accounted for this relationship or if cell fate patterning and developmental timing also contributed. Since *C. elegans* zygotes divide asymmetrically, patterning is already established at the 2-cell stage by asymmetric distribution of cell fate determinants (Nance, 2005; Rose and Kemphues, 1998). The first division of the *C. elegans* zygote produces a large anterior AB blastomere from which most somatic tissues emerge and a small posterior P1 blastomere from which the germline originates (Figure 2A) (Sulston et al., 1983). We used a fast acting temperature sensitive (ts) mutant of formin CYK-1 to induce cytokinesis failure in the zygote (Figure 2C) (Canman et al., 2008; Davies et al., 2014). In control 2-cell stage embryos, AB and P1 blastomeres display shorter spindles than the 1-celled zygote, which correlates with slower microtubule growth in both blastomeres (Figure 2D). At the restrictive temperature (26°C), *cyk-1(ts)* mutant zygotes exhibit cytokinesis failure and form abnormal 1-cell embryos that kinetically correspond to 2-cell stage embryos but possess the cytoplasmic content and cell fate determinants of both AB and P1 blastomeres. These abnormal embryos assembled tetrapolar spindles with microtubules that grew at a rate indistinguishable from normal 1-cell zygotes (Figure 2C,D). So, cell fate determinants and developmental timing do not make a major contribution to set the spindle microtubule growth rate in cleaving *C. elegans* embryos. To further demonstrate the effect of cell volume on spindle microtubule growth rate, we generated abnormally large zygotes. We generated embryos depleted of the fucosyltransferase C27D9.1, which does not have any known direct effect on microtubules and leads to the formation of abnormally large embryos (Hara and Kimura, 2009; Sonnichsen et al., 2005). In these extra-large zygotes, we found longer spindles and a significantly higher growth rate of spindle microtubules than in control normal-sized zygotes (Figure 2C,D). Altogether, these results show that the observed progressive reduction in the growth rate of spindle

microtubules is directly linked to cell volume during embryonic cleavage and independent of developmental timing or cell fate.

Spindle Length Scales with Microtubule Growth Rate in *C. elegans*

We then asked if variations between dynamics parameters of astral and spindle microtubules and cell volume could underlie spindle length scaling during early embryogenesis. Strikingly, we found that the growth rate of both astral and spindle microtubules was the only parameter exhibiting a distinct, progressive and linear decrease with spindle length throughout cleavage (Figure 3A-C). This observation suggests that modulating the growth rate of one or both microtubule populations could be a key determinant for spindle length adaptation in cleaving embryos. However, analysis of this scaling in C27D9.1-depleted extra-large zygotes revealed that only spindle microtubule growth rate increased with spindle length (Figure 3B), while astral microtubule growth rate remained similar to controls (Figure 3C) ($0.41 \pm 0.08 \mu\text{m/s}$ versus $0.40 \pm 0.09 \mu\text{m/s}$, $p=0.087$ unpaired t-test). These results suggest that spindle, but not astral, microtubule dynamics determine spindle length in cleaving embryos.

As the growth rate of spindle microtubules decreased progressively with cell volume during embryo cleavage and concomitant with spindle length, we hypothesized that modulating this parameter is sufficient to scale spindle length to cell volume during embryo cleavage. We calculated the average length $\langle L \rangle$ predicted from microtubule dynamics parameters (Figure 3D, S2B,C and Table S1)(Verde et al., 1992). In control embryos, $\langle L \rangle$ scaled linearly with our experimentally measured spindle lengths from the 1- to the 16-cell stage. This scaling implies that spindle length is a multiple of $\langle L \rangle$ and that the multiplicative factor remains relatively constant as cell size evolves. Interestingly, the predicted average length $\langle L \rangle$ of spindle microtubules in C27D9.1-depleted embryos fitted well with the abnormally long spindles in

these extra-large zygotes. Thus, spindle length varies proportionally to the overall microtubule dynamics in cleaving embryos. Since rescue frequency is low but catastrophe frequency and shrinkage rate are almost constant in cleaving *C. elegans* embryos, our results demonstrate that $\langle L \rangle$ is primarily determined by the microtubule growth rate (Figure 3B,D and Table S1). Our results support the idea that spindle microtubule growth rate is a key regulator to scale spindle length to cell volume.

To directly test this hypothesis, we experimentally reduced spindle microtubule growth rate in zygotes and measured spindle length. We analyzed zygotes partially depleted of the microtubule-associated protein (MAP) CLS-2 (ortholog of CLASP, Figure 3A-C) (Cheeseman et al., 2005; Espiritu et al., 2012), since CLS-2 promotes microtubule assembly *in vitro* and *in vivo* (Maton et al., 2015). Consistent with this, in partial *cls-2(RNAi)* conditions, spindle microtubules displayed a significantly reduced growth rate compared to in control zygotes (0.25 ± 0.06 versus $0.3 \pm 0.07 \mu\text{m/s}$, $p < 0.001$ unpaired t-test) (Figure 3B and Table S1). Rescue frequency also slightly increased, while catastrophe frequency and shrinkage rate remained unaltered. As we predicted, abnormally short but functional spindles assembled under this condition. Strikingly, both the average theoretical length of microtubules $\langle L \rangle$ and spindle length in these depleted zygotes were concomitantly reduced to levels corresponding to that of 4-cell stage control blastomeres (Figure 3B-D). Taken together, our results show that microtubule dynamics parameters, specifically the growth rate of spindle microtubules, vary proportionally to cell volume and are key factors that control spindle length during *C. elegans* embryo cleavage.

Spindle Length and Microtubule Growth Rate Scale with Cell Volume in the Sea Urchin *P. lividus*

We next wanted to investigate whether the scaling relationship among cell volume, spindle length, and microtubule growth rate identified in *C. elegans* is conserved in other species. Sea urchin (*Paracentrotus lividus*) embryos are approximately 15 times larger in volume than *C. elegans* embryos. *P. lividus* zygotes are spherical and divide symmetrically and synchronously until the 8-cell stage (Figure 4A) (Agrell, 1956; Parisi et al., 1978). First, we microinjected *P. lividus* oocytes with fluorescently labeled tubulin, which then underwent fertilization. We examined the first six rounds of embryonic cleavages by live confocal microscopy (Movie S1). Consistent with previous reports for other echinoderms (Crowder et al., 2015), spindle length and cell volume progressively decreased across early embryogenesis in *P. lividus* (Figure S4 and Table S2). To determine if microtubule dynamics also varied concomitantly with spindle length and cell volume, we generated kymographs of individual microtubules to measure spindle microtubule dynamics parameters. In line with our results from *C. elegans* embryos, microtubule dynamics parameters varied during *P. lividus* cleavage, but the overall microtubule dynamics remained in the bounded regime at every stage (Figure 4B and Table S2). We observed a continuous and significant decrease in the growth rate of spindle microtubules across *P. lividus* embryo cleavage (Figure 4B). This decrease correlated with the progressive reduction in blastomere volume and spindle length (Figure 4C,D). These results suggest microtubule growth rate is a key determinant of spindle length in cleaving sea urchin embryos. Importantly, both spindle length and spindle microtubule growth rate were comparable in vegetal micromeres (which result from strong asymmetric division at the 8-cell stage and inherit a fate determining polar domain (Angerer and Angerer, 2000; Davidson et al., 1998)) and in 32-cell stage blastomeres at the animal pole ($p=0.85$ unpaired t-test, Figure 4A,B). Thus, cell volume, but not cell fate or developmental timing, appears to dictate spindle microtubule growth

rate and consequent spindle size in cleaving *P. lividus* embryos, as we found for *C. elegans*. We conclude that this scaling principle operates across a 500-fold change in cell volume and could represent an evolutionarily conserved feature of cleaving embryos.

3D Simulations Reproduce Spindle Length Scaling with Microtubule Growth Rate

To directly test if modulating only microtubule growth rate is sufficient for spindle length scaling, we utilized computer simulations. Using the cytoskeletal simulator Cytosim to develop a three-dimensional spindle model, we examined the contribution of the microtubule growth rate on spindle size in a dose-dependent manner *in silico* (www.cytosim.org, (Nedelec F, 2007)). We modeled each spindle pole as an aster composed of a preset number of microtubules that can grow, shrink and stochastically undergo catastrophe and rescue (Figure 5A and S5, see detailed parameters in Table S3 and Methods). We constructed the aster by distributing a subset of these microtubules evenly and then confining the remaining microtubules within a cone that reproduced the higher microtubule density that grows toward the metaphase plate in *C. elegans* spindles. We represented the metaphase plate itself using a fixed volume in the center of the cell that microtubules cannot enter. Using our experimental measurements, we scaled cell volume, metaphase plate thickness and spindle width linearly with respect to the input growth rate (Table S2B). Growing microtubules emanating from the two centrosomes could exert pushing forces against the metaphase plate, so these forces would push spindle poles apart leading to spindle elongation. To ensure that spindle pole movements would strictly occur through growing microtubules pushing on the cell cortex or on the metaphase plate, we omitted microtubule motors from this model. We analyzed the effects of modulating the microtubule growth rate as a function of cell volume, while the three other microtubule dynamics parameters remained constant. We tested a physiological range of microtubule growth rates we measured *in vivo* in *C.*

elegans (Table S1). In this first set of simulations, the spindle length (pole-to-pole distance) trended toward a plateau over time at every tested microtubule growth rate (Figure 5B and Movie S2). Consistent with our hypothesis, the steady state spindle length decreased concomitantly with the microtubule growth rate (Figure 5C). Overall, the spindle lengths calculated *in silico* were in good agreement with our experimental measurements (Figure 5C), which confirms that this simple model accurately recapitulated the *in vivo* relationship between microtubule growth rate and spindle length.

Since our experimental data suggested that spindle length correlates with spindle, but not astral microtubule dynamics, we tested if a simulation devoid of cell boundary and astral microtubules could reproduce the relationship between spindle length and microtubule growth rate (Figure 5D). So, we tested a range of microtubule growth rates, while keeping all other parameters constant (Figure 5E and Movie S3). We did find that spindle length plateaued over time at a length that increased with microtubule growth rate that yielded similar values and scaling slopes as in our experiments (Figure 5F). This model exhibited the correct multiplicative factor between $\langle L \rangle$ and spindle length, which suggests that this scaling factor only depends on the geometrical dimensions of the system (i.e. cell size and/or dimensions of the metaphase plate) included in the simulation. Together, these findings suggest that modulating spindle microtubule growth rate is a sufficient determinant of spindle size scaling with cell volume in cleaving embryos.

Spindle Assembly and Microtubule Growth Rates Proportionally Correlate with Constant

Spindle Assembly Timing During Embryo Cleavage

A striking finding from our 3D simulations was that spindle length reached steady state within a timeframe that was independent of microtubule growth rate or final spindle size (Figure

5B, E and S5D). So, our simulations predict that shorter spindles would not assemble faster than longer ones. To test if this occurred *in vivo*, we compared spindle lengths at various stages of *C. elegans* cleavage with the timing of spindle assembly (Figure 6A and Movie S4). Since spindle length continuously increases from NEBD to anaphase onset in *C. elegans* embryos, we approximated spindle assembly timing as the duration between NEBD and anaphase onset. We found that the timing of spindle assembly was independent of the initial distance between centrosomes or final spindle length (Figure 6B). Although spindle assembly took slightly longer in the 1-celled zygote than in subsequent stages, spindle assembly durations stayed relatively constant over the first five rounds of embryonic division, despite the progressive decrease in spindle length at each division. We also observed a progressive decrease of the spindle assembly rate, which strongly correlated with the decreasing spindle length and microtubule growth rate across early embryonic divisions (including in the zygote, Figure 6C and D). These results agree with the predictions from our simulations. Therefore, the progressive decrease of the microtubule growth rate is sufficient to regulate the constant timing of spindle assembly in cleaving embryos.

Discussion

In summary, we explored the dynamic properties of microtubules as cell size decreases in early cleaving embryos. Using the nematode *C. elegans* and the sea urchin *P. lividus*, our results establish that the growth rate of spindle microtubules in both species is the primary determinant of dynamic instability that decreases proportionally to cell volume and concomitantly with spindle length. Using an *in silico* 3D spindle model, we demonstrate that modulating the microtubule growth rate is sufficient to control spindle size and recapitulate spindle length scaling with respect to cell volume. Our results suggest a conserved mechanism to adjust spindle length with varying cell volume, as typically found in early embryonic development. Importantly, our results elucidate how spindle assembly timing is constant among different blastomere sizes in early embryos. This mechanism may be crucial to prevent chromosome segregation defects and aneuploidy.

Microtubule Dynamics and Spindle Length

Our analysis revealed that the microtubule growth rate decreases proportionally to spindle length based on cell volume across reductive divisions in early *C. elegans* and *P. lividus* embryos. This contrasts with previous work comparing stage 3 and 8 *Xenopus* embryo extracts. These studies found no major variation in the microtubule growth rate, but a threefold increase in the microtubule catastrophe frequency correlated with smaller spindles (Wilbur and Heald, 2013). Taken together, different mechanisms may exist across phylogeny to regulate microtubule dynamics as a function of cell volume that produce similar effects on spindle length. This assertion could simply reflect evolutionary diversity. However, we note that *Xenopus* blastomeres (at both stages 3 and 8) are significantly larger than *C. elegans* or *P. lividus* embryos, which could favor one spindle scaling mechanism over the other. Moreover, stage 8

blastomeres utilize a linear scaling regime, where spindle length scales linearly with cell size, while stage 3 blastomeres remain in the ‘large-cell’ regime, in which spindle length reaches an upper limit and is uncoupled from cell size (Wilbur and Heald, 2013; Wuhr et al., 2008). In the ‘large-cell’ regime, spindle length is controlled through spindle intrinsic mechanisms (Mitchison et al., 2015). The difference in the catastrophe frequency between stage 3 and 8 could be related to the transitioning from ‘large-cell’ to linear scaling regime rather than reflecting a cell size-dependent spindle scaling mechanism. Finally, results obtained with *Xenopus* egg extracts could also follow the removal of membrane confinements.

We still must determine the specific factors that control microtubule growth rate with respect to cell volume. The limiting component hypothesis proposes that one or several factors, critical for spindle assembly have a limited supply, so their absolute quantity per cell diminishes upon embryo cleavage (Mitchison et al., 2015; Reber and Goehring, 2015). Tubulin is the most obvious candidate, as its concentration does determine the rate of microtubule elongation *in vitro* (Walker et al., 1988). However, several *in vitro* and *in vivo* studies argue against tubulin being the sole limiting component. In *Xenopus* egg extracts or in the presence of crowding agent *in vitro*, the growth rate of microtubules is not linearly dependent on the available tubulin concentration (Parsons and Salmon, 1997; Wieczorek M, 2013), as robust spindle length scaling occurred in lipid droplets even after artificially increasing the amount of tubulin (Good et al., 2013). In sea urchin embryos, a 5-fold excess of tubulin is present in a soluble non-polymerized form, which can be artificially mobilized into the spindle upon treatment with crowding agents (Inoue and Sato, 1967; Raff et al., 1975; Raff and Kaumeyer, 1973; Rebhun et al., 1975), which indicates that tubulin itself is not limiting in this system. Our results using quantitative western blotting estimated a tubulin concentration of approximately 22 μM in *C. elegans* embryos, which

is similar to *Xenopus* embryos (Figure S6, (Belmont et al., 1990)). Based on a recent study providing the first complete electron tomographic reconstruction of the mitotic spindle in the *C. elegans* zygote (Redemann et al., 2017), we estimated that the total amount of tubulin heterodimers should be sufficient to assemble 2–3 zygotic mitotic spindles (see Methods). Overall, tubulin seems unlikely to be the only limiting factor for spindle length scaling. Another possibility is that specific microtubule-associated proteins (MAPs) that regulate microtubule growth rate are also limiting. Consistent with this, we found that reducing levels of the CLS-2 protein in *C. elegans* zygotes modulated microtubule growth rate and spindle length proportionally. However, MAPs influence several microtubule dynamics parameters, which complicates the identification of the key factor(s) that coordinates spindle length with cell size in early embryos *in vivo* (Bowne-Anderson et al., 2015).

Microtubule Dynamics and Cell Volume

Parameters of microtubule dynamics scaled similarly across cleavages in *C. elegans* and *P. lividus* but had different absolute values in the two species. *C. elegans* embryos are ~15 times smaller in volume than sea urchin embryos, but their microtubules grow significantly faster at every stage of cleavage (Figure S7A). These results indicate that microtubule growth rate is not an absolute predictor of spindle length (Figure S7B-D). In contrast, the average theoretical microtubule length $\langle L \rangle$, calculated from the four parameters of dynamic instability, is a good predictor. When plotted against cell volume, $\langle L \rangle$ followed a linear and similar trend in both species (Figure S7F). Strikingly, blastomeres of comparable volumes displayed very similar values of $\langle L \rangle$ regardless of their species of origin (*C. elegans* 2-cell stage blastomeres and *P. lividus* 32-cell stage blastomeres display volumes of 10.6 and 9.28 pl respectively and $\langle L \rangle$ of 2.48 and 2.42 μm respectively). $\langle L \rangle$ is a readout of the overall microtubule dynamics, which

suggests that microtubule dynamics vary to set an average microtubule length that scales with cell volume. Furthermore, since spindle length is roughly proportional to $\langle L \rangle$, microtubule dynamics are modulated to scale spindle length with cell volume.

However, we note that $\langle L \rangle$ is not equal to the spindle half-length nor do we suggest that spindle length is solely determined by microtubule length. Spindle assembly requires other factors (Dumont and Mitchison, 2009b; Mitchison et al., 2015; Reber and Hyman, 2015; Walczak and Heald, 2008; Waters and Salmon, 1997). We also provide evidence for premise, as $\langle L \rangle$ did not always scale linearly with spindle length in *P. lividus* (Figure S7E). Specifically, 1- and 2-cell stage sea urchin blastomeres deviated from the linear scaling trend followed by other cells, and assembled spindles that were shorter than predicted by values of $\langle L \rangle$. Several non-exclusive causes could account for the discrepancy between $\langle L \rangle$ and spindle length: microtubules may bend, detach from the centrosomes or be severed (Brangwynne et al., 2006; Crowder et al., 2015; Dumont and Mitchison, 2009a; Gadde and Heald, 2004; Goshima et al., 2005a; Maiato et al., 2004; McBeath and Fujiwara, 1990; Reber and Hyman, 2015; Redemann et al., 2017; Wuhr et al., 2008). We also note that theoretically microtubule growth rate should regulate microtubule mass within the spindle rather than the spindle length itself (Mitchison et al., 2015; Reber et al., 2013). So, when microtubule length and spindle length scale linearly together, microtubule mass should also scale linearly. But in larger blastomeres, an excess in microtubule mass, due to the increased growth rate, could be compensated by a change in spindle shape rather than length. Consistent with this later possibility and observations from embryos in other species (Crowder et al., 2015; Hara and Kimura, 2013), we observed a significant change in the spindle length to width ratio and in the centrosome radius in *P. lividus* among cleavages,

which correlated with proportionally wider spindle poles at earlier stages (Figure S4B and Table S2).

Microtubule Dynamics and Spindle Assembly Rate

In addition to spindle size, we also found that the rate of spindle assembly scaled with cell size in *C. elegans* embryos. Our simulations combined with our *in vivo* measurements suggest that this scalability occurs through the proportional relationship between microtubule growth rate and steady state spindle length. This property could be key in early embryos that undergo rapid cell divisions with a weak spindle assembly checkpoint (Encalada et al., 2005). Indeed, *C. elegans* embryos respond to unattached kinetochores by inducing a small delay in mitosis but do not arrest their cell cycle progression. In this context, adapting the microtubule growth rate to the final spindle length would ensure efficient chromosome biorientation and avoid sister chromatid mis-segregation. In particular, the ‘search-and-capture’ model (Kirschner and Mitchison, 1986) predicts that the search for kinetochores is optimal when the average microtubule length equals the distance at which chromosomes are located (Holy and Leibler, 1994). When this condition is satisfied, the capture time scales with the inverse of the catastrophe frequency. Thus, scaling the microtubule growth rate with a nearly constant catastrophe frequency corresponds to a global optimization of the search-and-capture strategy, since the overall time required for search-and-capture remains constant during embryonic cleavage. So, fast-assembling microtubules in large blastomeres reach further and search more space to ensure timely chromosome capture during the short mitotic time window. As cleavage progresses and spindle length decreases, slowing down microtubule assembly may negate the simultaneous connection of individual kinetochores to both spindle poles, which would promote merotelly and gross chromosome segregation if not corrected. From these observations, we

envision that decreasing the microtubule growth rate permits the embryo to not only scale down its spindles, but also globally optimize chromosome segregation during embryogenesis. Previous work in *C. elegans* embryos demonstrated that the rate of spindle elongation during anaphase (Hara and Kimura, 2009) and the rate of cortical ring constriction during cytokinesis (Carvalho et al., 2009) also decreased as cell volume decreased, which makes the time needed for anaphase spindle elongation and for cytokinetic ring constriction independent of cell size. Future studies should examine whether the rates of other cell division processes also exhibit intrinsic scalability and whether this is a general principle that dictates how cell biological processes scale with cell size.

AUTHOR CONTRIBUTIONS

B.L. and J.D. conceived the project with input from all authors. B.L. performed all of the experiments, except those specifically attributed to other authors. L.P. performed the CL β L experiments and analysis. J.S. and N.M. performed the sea urchin microinjection experiments. G.M. performed the *C. elegans* microinjection experiments. M.S. and J.C.C. generated some strains used in this study. A.M.L. performed some image analyses. B.L., J.D., G.L. and F.N. conceived the *in silico* model, and G.L. and F.N. extended Cytosim to implement it. G.L. performed the computer simulations under supervision of F.N. B.L. and J.D. made the figures and wrote the manuscript with input from all authors.

ACKNOWLEDGMENTS

We thank all members of the Dumont lab for support and advice. We are grateful to Patricia Moussounda for providing technical support. We thank Life Science Editors for editing assistance. We acknowledge the ImagoSeine core facility of the Institut Jacques Monod, member of IBiSA and France-BioImaging (ANR-10-INBS-04) infrastructures. We thank Nicolas Tissot (ImagoSeine) for his help with the 2-photon microscopy. We thank Julie Ahringer (The Gurdon Institute, University of Cambridge, UK) for the generous gift of the JA1559 *C. elegans* strain. Some strains were provided by the CGC, which is funded by NIH Office of Research Infrastructure Programs (P40 OD010440). We thank Dmitry Ershov (IJM, Paris, France) for his help with MATLAB. We are grateful to Jean-Claude Labbe (IRIC) for initial technical support and discussions. B.L. was originally supported by a post-doctoral fellowship from the *Fondation pour la Recherche Médicale* (FRM ARF20140129055). This work was supported by CNRS and University Paris Diderot and by grants from the *Agence Nationale pour la Recherche* (ANR-16-

CE13-0020-01), the *Mairie de Paris* (Emergence) and the *Fondation pour la Recherche Médicale* (FRM DEQ20160334869) to J.D.

SUPPLEMENTARY MOVIE LEGENDS

Movie S1. Microtubule dynamics in a cleaving *Paracentrotus lividus* embryo. Related to Figure 4.

Movie from live confocal acquisitions of a 16-cell stage *P. lividus* embryo microinjected with ATTO 565-tubulin (grey). A single focal plane was imaged every second. Scale bar, 20 μm .

Movie S2. *In silico* assembly of a steady-state length mitotic spindle in a confined space with astral microtubules. Related to Figure 5.

Movie from a simulation made with Cytosim as presented in Figure 5A-C. Input microtubule growth rate in this simulation is 0.35 $\mu\text{m/s}$. Scale bar, 10 μm .

Movie S3. *In silico* assembly of a steady-state length mitotic spindle in an infinite space and without astral microtubules. Related to Figure 5.

Movie from a simulation made with Cytosim, as presented in Figure 6D-F. Input microtubule growth rate in this simulation is 0.31 $\mu\text{m/s}$. Scale bar, 10 μm .

Movie S4. Timing of spindle assembly during *C. elegans* embryo cleavage. Related to Figure 6.

Combined stacks from live confocal imaging of *C. elegans* embryos co-expressing mCherry-tagged Histone H2B (Magenta) and GFP-tagged β -tubulin (Grey) during spindle assembly in the first six embryonic divisions (1- to 32-cell stage from left to right). Movies correspond to maximum intensity projection of z-stacks. Movies start 15 s prior to NEBD and end after anaphase onset. Note that spindle assembly takes slightly more time in the 1-cell embryo. Scale bar, 10 μm .

DECLARATION OF INTERESTS

The authors declare no competing interests.

REFERENCES

Agrell, I. (1956). A mitotic gradient as the cause of the early differentiation in the sea urchin embryo. *Zoological Papers in Honour of B Hanstrom*, pp. 27-34.

Andersen, S.S. (2000). Spindle assembly and the art of regulating microtubule dynamics by MAPs and Stathmin/Op18. *Trends Cell Biol* 10, 261-267.

Andersen, S.S., Ashford, A.J., Tournebize, R., Gavet, O., Sobel, A., Hyman, A.A., and Karsenti, E. (1997). Mitotic chromatin regulates phosphorylation of Stathmin/Op18. *Nature* 389, 640-643.

Angerer, L.M., and Angerer, R.C. (2000). Animal-vegetal axis patterning mechanisms in the early sea urchin embryo. *Dev Biol* 218, 1-12.

Belmont, L.D., Hyman, A.A., Sawin, K.E., and Mitchison, T.J. (1990). Real-time visualization of cell cycle-dependent changes in microtubule dynamics in cytoplasmic extracts. *Cell* 62, 579-589.

Bowne-Anderson, H., Hibbel, A., and Howard, J. (2015). Regulation of Microtubule Growth and Catastrophe: Unifying Theory and Experiment. *Trends Cell Biol* 25, 769-779.

Brangwynne, C.P., MacKintosh, F.C., Kumar, S., Geisse, N.A., Talbot, J., Mahadevan, L., Parker, K.K., Ingber, D.E., and Weitz, D.A. (2006). Microtubules can bear enhanced compressive loads in living cells because of lateral reinforcement. *J Cell Biol* 173, 733-741.

Brenner, S. (1974). The genetics of *Caenorhabditis elegans*. *Genetics* 77, 71-94.

Brown, K.S., Blower, M.D., Maresca, T.J., Grammer, T.C., Harland, R.M., and Heald, R. (2007). *Xenopus tropicalis* egg extracts provide insight into scaling of the mitotic spindle. *J Cell Biol* 176, 765-770.

Canman, J.C., Lewellyn, L., Laband, K., Smerdon, S.J., Desai, A., Bowerman, B., and Oegema, K. (2008). Inhibition of Rac by the GAP activity of centralspindlin is essential for cytokinesis. *Science* 322, 1543-1546.

Carvalho, A., Desai, A., and Oegema, K. (2009). Structural memory in the contractile ring makes the duration of cytokinesis independent of cell size. *Cell* 137, 926-937.

Castoldi, M., and Popov, A.V. (2003). Purification of brain tubulin through two cycles of polymerization-depolymerization in a high-molarity buffer. *Protein Expr Purif* 32, 83-88.

Chalfie, M., and Thomson, J.N. (1982). Structural and functional diversity in the neuronal microtubules of *Caenorhabditis elegans*. *J Cell Biol* 93, 15-23.

Chan, Y.H., and Marshall, W.F. (2010). Scaling properties of cell and organelle size. *Organogenesis* 6, 88-96.

Chan, Y.H., and Marshall, W.F. (2012). How cells know the size of their organelles. *Science* 337, 1186-1189.

Cheeseman, I.M., MacLeod, I., Yates, J.R., 3rd, Oegema, K., and Desai, A. (2005). The CENP-F-like proteins HCP-1 and HCP-2 target CLASP to kinetochores to mediate chromosome segregation. *Curr Biol* 15, 771-777.

Crowder, M.E., Strzelecka, M., Wilbur, J.D., Good, M.C., von Dassow, G., and Heald, R. (2015). A comparative analysis of spindle morphometrics across metazoans. *Curr Biol* 25, 1542-1550.

Davidson, E.H., Cameron, R.A., and Ransick, A. (1998). Specification of cell fate in the sea urchin embryo: summary and some proposed mechanisms. *Development* *125*, 3269-3290.

Davies, T., Jordan, S.N., Chand, V., Sees, J.A., Laband, K., Carvalho, A.X., Shirasu-Hiza, M., Kovar, D.R., Dumont, J., and Canman, J.C. (2014). High-resolution temporal analysis reveals a functional timeline for the molecular regulation of cytokinesis. *Dev Cell* *30*, 209-223.

Decker, M., Jaensch, S., Pozniakovsky, A., Zinke, A., O'Connell, K.F., Zachariae, W., Myers, E., and Hyman, A.A. (2011). Limiting amounts of centrosome material set centrosome size in *C. elegans* embryos. *Curr Biol* *21*, 1259-1267.

Desai, A., and Mitchison, T.J. (1997). Microtubule polymerization dynamics. *Annu Rev Cell Dev Biol* *13*, 83-117.

Dogterom, M., and Yurke, B. (1997). Measurement of the force-velocity relation for growing microtubules. *Science* *278*, 856-860.

Dumont, S., and Mitchison, T.J. (2009a). Compression regulates mitotic spindle length by a mechanochemical switch at the poles. *Curr Biol* *19*, 1086-1095.

Dumont, S., and Mitchison, T.J. (2009b). Force and length in the mitotic spindle. *Curr Biol* *19*, R749-761.

Encalada, S.E., Willis, J., Lyczak, R., and Bowerman, B. (2005). A spindle checkpoint functions during mitosis in the early *Caenorhabditis elegans* embryo. *Mol Biol Cell* *16*, 1056-1070.

Espiritu, E.B., Krueger, L.E., Ye, A., and Rose, L.S. (2012). CLASPs function redundantly to regulate astral microtubules in the *C. elegans* embryo. *Dev Biol* *368*, 242-254.

Fire, A., Xu, S., Montgomery, M.K., Kostas, S.A., Driver, S.E., and Mello, C.C. (1998). Potent and specific genetic interference by double-stranded RNA in *Caenorhabditis elegans*. *Nature* *391*, 806-811.

Frokjaer-Jensen, C., Davis, M.W., Hopkins, C.E., Newman, B.J., Thummel, J.M., Olesen, S.P., Grunnet, M., and Jorgensen, E.M. (2008). Single-copy insertion of transgenes in *Caenorhabditis elegans*. *Nat Genet* *40*, 1375-1383.

Gadde, S., and Heald, R. (2004). Mechanisms and molecules of the mitotic spindle. *Curr Biol* *14*, R797-805.

Gittes, F., Mickey, B., Nettleton, J., and Howard, J. (1993). Flexural rigidity of microtubules and actin filaments measured from thermal fluctuations in shape. *J Cell Biol* *120*, 923-934.

Goehring, N.W., and Hyman, A.A. (2012). Organelle growth control through limiting pools of cytoplasmic components. *Curr Biol* *22*, R330-339.

Good, M.C., Vahey, M.D., Skandarajah, A., Fletcher, D.A., and Heald, R. (2013). Cytoplasmic volume modulates spindle size during embryogenesis. *Science* *342*, 856-860.

Goshima, G., Nedelec, F., and Vale, R.D. (2005a). Mechanisms for focusing mitotic spindle poles by minus end-directed motor proteins. *J Cell Biol* *171*, 229-240.

Goshima, G., Wollman, R., Stuurman, N., Scholey, J.M., and Vale, R.D. (2005b). Length control of the metaphase spindle. *Curr Biol* *15*, 1979-1988.

Greenan, G., Brangwynne, C.P., Jaensch, S., Gharakhani, J., Julicher, F., and Hyman, A.A. (2010). Centrosome size sets mitotic spindle length in *Caenorhabditis elegans* embryos. *Curr Biol* *20*, 353-358.

Hara, Y., and Kimura, A. (2009). Cell-size-dependent spindle elongation in the *Caenorhabditis elegans* early embryo. *Curr Biol* *19*, 1549-1554.

Hara, Y., and Kimura, A. (2013). An allometric relationship between mitotic spindle width, spindle length, and ploidy in *Caenorhabditis elegans* embryos. *Mol Biol Cell* *24*, 1411-1419.

Hazel, J., Krutkramelis, K., Mooney, P., Tomschik, M., Gerow, K., Oakey, J., and Gatlin, J.C. (2013). Changes in cytoplasmic volume are sufficient to drive spindle scaling. *Science* 342, 853-856.

Holmfeldt, P., Brannstrom, K., Stenmark, S., and Gullberg, M. (2006). Aneugenic activity of Op18/stathmin is potentiated by the somatic Q18-->e mutation in leukemic cells. *Mol Biol Cell* 17, 2921-2930.

Holy, T.E., and Leibler, S. (1994). Dynamic instability of microtubules as an efficient way to search in space. *Proc Natl Acad Sci U S A* 91, 5682-5685.

Hyman, A.A. (1991). Preparation of marked microtubules for the assay of the polarity of microtubule-based motors by fluorescence. *J Cell Sci Suppl* 14, 125-127.

Inoue, S., and Sato, H. (1967). Cell motility by labile association of molecules. The nature of mitotic spindle fibers and their role in chromosome movement. *J Gen Physiol* 50, Suppl:259-292.

Janson, M.E., de Dood, M.E., and Dogterom, M. (2003). Dynamic instability of microtubules is regulated by force. *J Cell Biol* 161, 1029-1034.

Kamath, R.S., Martinez-Campos, M., Zipperlen, P., Fraser, A.G., and Ahringer, J. (2001). Effectiveness of specific RNA-mediated interference through ingested double-stranded RNA in *Caenorhabditis elegans*. *Genome Biol* 2, RESEARCH0002.

Kirschner, M., and Mitchison, T. (1986). Beyond self-assembly: from microtubules to morphogenesis. *Cell* 45, 329-342.

Kole, T.P., Tseng, Y., Jiang, I., Katz, J.L., and Wirtz, D. (2005). Intracellular mechanics of migrating fibroblasts. *Mol Biol Cell* 16, 328-338.

Labbe, J.C., McCarthy, E.K., and Goldstein, B. (2004). The forces that position a mitotic spindle asymmetrically are tethered until after the time of spindle assembly. *J Cell Biol* 167, 245-256.

Lacroix, B., and Maddox, A.S. (2014). Microtubule dynamics followed through cell differentiation and tissue biogenesis in *C. elegans*. *Worm* 3, e967611.

Lacroix, B., Ryan, J., Dumont, J., Maddox, P.S., and Maddox, A.S. (2016). Identification of microtubule growth deceleration and its regulation by conserved and novel proteins. *Mol Biol Cell* 27, 1479-1487.

Lancaster, O.M., Le Berre, M., Dimitracopoulos, A., Bonazzi, D., Zlotek-Zlotkiewicz, E., Picone, R., Duke, T., Piel, M., and Baum, B. (2013). Mitotic rounding alters cell geometry to ensure efficient bipolar spindle formation. *Dev Cell* 25, 270-283.

Letort, G., Nedelec, F., Blanchoin, L., and Thery, M. (2016). Centrosome centering and decentering by microtubule network rearrangement. *Mol Biol Cell* 27, 2833-2843.

Levy, D.L., and Heald, R. (2012). Mechanisms of intracellular scaling. *Annu Rev Cell Dev Biol* 28, 113-135.

Loughlin, R., Wilbur, J.D., McNally, F.J., Nedelec, F.J., and Heald, R. (2011). Katanin contributes to interspecies spindle length scaling in *Xenopus*. *Cell* 147, 1397-1407.

Maddox, P., Straight, A., Coughlin, P., Mitchison, T.J., and Salmon, E.D. (2003). Direct observation of microtubule dynamics at kinetochores in *Xenopus* extract spindles: implications for spindle mechanics. *J Cell Biol* 162, 377-382.

Maiato, H., Rieder, C.L., and Khodjakov, A. (2004). Kinetochore-driven formation of kinetochore fibers contributes to spindle assembly during animal mitosis. *J Cell Biol* 167, 831-840.

Marshall, W.F. (2015a). How Cells Measure Length on Subcellular Scales. *Trends Cell Biol* 25, 760-768.

Marshall, W.F. (2015b). Subcellular size. *Cold Spring Harb Perspect Biol* 7.

Maton, G., Edwards, F., Lacroix, B., Stefanutti, M., Laband, K., Lieury, T., Kim, T., Espeut, J., Canman, J.C., and Dumont, J. (2015). Kinetochore components are required for central spindle assembly. *Nat Cell Biol* 17, 697-705.

McBeath, E., and Fujiwara, K. (1990). Microtubule detachment from the microtubule-organizing center as a key event in the complete turnover of microtubules in cells. *Eur J Cell Biol* 52, 1-16.

Mitchison, T., and Kirschner, M. (1984). Dynamic instability of microtubule growth. *Nature* 312, 237-242.

Mitchison, T.J., Ishihara, K., Nguyen, P., and Wuhr, M. (2015). Size Scaling of Microtubule Assemblies in Early *Xenopus* Embryos. *Cold Spring Harb Perspect Biol* 7, a019182.

Muller-Reichert, T., Greenan, G., O'Toole, E., and Srayko, M. (2010). The elegans of spindle assembly. *Cell Mol Life Sci* 67, 2195-2213.

Nance, J. (2005). PAR proteins and the establishment of cell polarity during *C. elegans* development. *Bioessays* 27, 126-135.

Nedelec F, F.D. (2007). Collective Langevin dynamics of flexible cytoskeletal fibers. *New J Phys* 9, 427-427.

Nogales, E., Wolf, S.G., and Downing, K.H. (1998). Structure of the alpha beta tubulin dimer by electron crystallography. *Nature* 391, 199-203.

O'Farrell, P.H., Stumpff, J., and Su, T.T. (2004). Embryonic cleavage cycles: how is a mouse like a fly? *Curr Biol* 14, R35-45.

Parisi, E., Filosa, S., De Petrocellis, B., and Monroy, A. (1978). The pattern of cell division in the early development of the sea urchin. *Paracentrotus lividus*. *Dev Biol* 65, 38-49.

Parsons, S.F., and Salmon, E.D. (1997). Microtubule assembly in clarified *Xenopus* egg extracts. *Cell Motil Cytoskeleton* 36, 1-11.

Picone, R., Ren, X., Ivanovitch, K.D., Clarke, J.D., McKendry, R.A., and Baum, B. (2010). A polarised population of dynamic microtubules mediates homeostatic length control in animal cells. *PLoS Biol* 8, e1000542.

Raff, R.A., Brandis, J.W., Green, L.H., Kaumeyer, J.F., and Raff, E.C. (1975). Microtubule protein pools in early development. *Ann N Y Acad Sci* 253, 304-317.

Raff, R.A., and Kaumeyer, J.F. (1973). Soluble microtubule proteins of the sea urchin embryo: partial characterization of the proteins and behavior of the pool in early development. *Dev Biol* 32, 309-320.

Reber, S., and Goehring, N.W. (2015). Intracellular Scaling Mechanisms. *Cold Spring Harb Perspect Biol* 7.

Reber, S., and Hyman, A.A. (2015). Emergent Properties of the Metaphase Spindle. *Cold Spring Harb Perspect Biol* 7, a015784.

Reber, S.B., Baumgart, J., Widlund, P.O., Pozniakovsky, A., Howard, J., Hyman, A.A., and Julicher, F. (2013). XMAP215 activity sets spindle length by controlling the total mass of spindle microtubules. *Nat Cell Biol* 15, 1116-1122.

Rebhun, L.I., Jemiole, D., Ivy, N., Mellon, M., and Nath, J. (1975). Regulation of the in vivo mitotic apparatus by glycols and metabolic inhibitors. *Ann N Y Acad Sci* 253, 362-377.

Redemann, S., Baumgart, J., Lindow, N., Shelley, M., Nazockdast, E., Kratz, A., Prohaska, S., Bragues, J., Furthauer, S., and Muller-Reichert, T. (2017). *C. elegans* chromosomes connect to centrosomes by anchoring into the spindle network. *Nat Commun* 8, 15288.

Rose, L.S., and Kempfues, K.J. (1998). Early patterning of the *C. elegans* embryo. *Annu Rev Genet* 32, 521-545.

Sonnichsen, B., Koski, L.B., Walsh, A., Marschall, P., Neumann, B., Brehm, M., Alleaume, A.M., Artelt, J., Bettencourt, P., Cassin, E., *et al.* (2005). Full-genome RNAi profiling of early embryogenesis in *Caenorhabditis elegans*. *Nature* 434, 462-469.

Srayko, M., Kaya, A., Stamford, J., and Hyman, A.A. (2005). Identification and characterization of factors required for microtubule growth and nucleation in the early *C. elegans* embryo. *Dev Cell* 9, 223-236.

Sulston, J.E., and Horvitz, H.R. (1977). Post-embryonic cell lineages of the nematode, *Caenorhabditis elegans*. *Dev Biol* 56, 110-156.

Sulston, J.E., Schierenberg, E., White, J.G., and Thomson, J.N. (1983). The embryonic cell lineage of the nematode *Caenorhabditis elegans*. *Dev Biol* 100, 64-119.

Tirnauer, J.S., Canman, J.C., Salmon, E.D., and Mitchison, T.J. (2002). EB1 targets to kinetochores with attached, polymerizing microtubules. *Mol Biol Cell* 13, 4308-4316.

Tournebize, R., Popov, A., Kinoshita, K., Ashford, A.J., Rybina, S., Pozniakovsky, A., Mayer, T.U., Walczak, C.E., Karsenti, E., and Hyman, A.A. (2000). Control of microtubule dynamics by the antagonistic activities of XMAP215 and XKCM1 in *Xenopus* egg extracts. *Nat Cell Biol* 2, 13-19.

Verde, F., Dogterom, M., Stelzer, E., Karsenti, E., and Leibler, S. (1992). Control of microtubule dynamics and length by cyclin A- and cyclin B-dependent kinases in *Xenopus* egg extracts. *J Cell Biol* 118, 1097-1108.

Verde, F., Labbe, J.C., Doree, M., and Karsenti, E. (1990). Regulation of microtubule dynamics by cdc2 protein kinase in cell-free extracts of *Xenopus* eggs. *Nature* 343, 233-238.

Walczak, C.E., and Heald, R. (2008). Mechanisms of mitotic spindle assembly and function. *Int Rev Cytol* 265, 111-158.

Walker, R.A., O'Brien, E.T., Pryer, N.K., Soboeiro, M.F., Voter, W.A., Erickson, H.P., and Salmon, E.D. (1988). Dynamic instability of individual microtubules analyzed by video light microscopy: rate constants and transition frequencies. *J Cell Biol* 107, 1437-1448.

Waters, J.C., and Salmon, E. (1997). Pathways of spindle assembly. *Curr Opin Cell Biol* 9, 37-43.

West, G.B., and Brown, J.H. (2005). The origin of allometric scaling laws in biology from genomes to ecosystems: towards a quantitative unifying theory of biological structure and organization. *J Exp Biol* 208, 1575-1592.

Wieczorek M, C.S., Brouhard G.J. (2013). Macromolecular Crowding Pushes Catalyzed Microtubule Growth to Near the Theoretical Limit. *Cellular and Molecular Bioengineering* 6, 383-392.

Wilbur, J.D., and Heald, R. (2013). Mitotic spindle scaling during *Xenopus* development by kif2a and importin alpha. *Elife* 2, e00290.

Wuhr, M., Chen, Y., Dumont, S., Groen, A.C., Needleman, D.J., Salic, A., and Mitchison, T.J. (2008). Evidence for an upper limit to mitotic spindle length. *Curr Biol* 18, 1256-1261.

FIGURE LEGENDS

Figure 1. Astral and Spindle Microtubule Dynamics Vary During *C. elegans* Embryo Cleavage

(A) Still frames from confocal live imaging of *C. elegans* embryos expressing GFP-tagged β -tubulin during the first five embryonic divisions (1- to 16-cell stage). Images correspond to a single focal plane. Scale bar, 20 μm .

(B) Schematic representation of microtubule dynamics parameter extraction from individual astral (green) or spindle (red) microtubule kymographs. One representative example of a kymograph shown of an individual astral microtubule tracked over time. Horizontal scale bars, 1 μm , vertical scale bar (kymograph), 5 s.

(C) Microtubule dynamics parameters for astral (green) and spindle (red) microtubules plotted at each cleavage stage (1- to 16-cell stage). Each dot corresponds to an individual microtubule. For both microtubule populations, each parameter significantly varies between stages (one-way ANOVA: $p < 0.01$). Only microtubule growth rates of both microtubule populations exhibit significant decrease at each stage (one-way ANOVA with Tukey's multiple comparison tests: $p < 0.01$). All parameters including sample size, mean and SD for the four astral and spindle microtubule dynamics parameters at the different stages are listed in Table S1. (Horizontal bars, means; error bars, SD; $n(\text{microtubules}) \geq 288$ per cleavage stage; $n(\text{embryos}) \geq 12$).

Figure 2. Astral and Spindle Microtubule Dynamics Vary with Cell Volume During *C. elegans* Embryo Cleavage

(A) Still frames from live 2-photon imaging of *C. elegans* embryos expressing a GFP-tagged plasma membrane probe (Pleckstrin Homology (PH) domain) during the first five embryonic divisions (1- to 16-cell stage). Images correspond to maximal projections of z-stacks covering the entire thickness of the embryo. Scale bar, 20 μm . Blastomere names are indicated except for the 16-cell stage. At the 8-cell stage, progeny of AB and P1 were grouped together as ABxx and P1xx respectively.

(B) Mean astral (green) and spindle (red) microtubule dynamics parameters: mean microtubule growth rate, catastrophe frequency, shrinkage rate and rescue frequency (from Figure 1C) for

each type of blastomere plotted over the corresponding average cell volumes (from Figure S1). Key for different blastomeres shown in the top box. Dotted lines correspond to the linear regression curves. Pearson correlation coefficient (r^2) is indicated at the top of each graph if $p \leq 0.01$ (no corr. is indicated otherwise).

(C) From left to right, still images from confocal live imaging of *C. elegans* control 1-cell embryo, control 2-cell embryo, thermosensitive (ts) mutant embryo of the formin *cyk-1* at the '2-cell' stage after P0 cytokinesis failure and abnormally large *C27D9.1(RNAi)*-treated embryo. All express GFP-tagged β -tubulin. Corresponding schematics with color-coding for spindle microtubules in different conditions shown at the bottom. Scale bar, 20 μm .

(D) Spindle microtubule growth rates measured at 25°C (restrictive temperature for the *cyk-1(ts)* mutant) for the indicated conditions. Color-coding for the different conditions corresponds to the schematics in (C). (Error bars, SD; one-way ANOVA with Dunnett's multiple comparisons test, **: $p \leq 0.01$, n.s.: $p > 0.05$).

Figure 3. Spindle Length Scales with Spindle, but not Astral, Microtubule Growth Rate

(A) From top to bottom, still images from confocal live imaging of *C. elegans* control 1-cell embryo, abnormally large *C27D9.1(RNAi)*-treated embryo and *cls-2(RNAi)*-treated embryo. All expressing GFP-tagged β -tubulin. Corresponding schematics with color-coding for astral and spindle microtubules in the different conditions shown underneath each image. Scale bar, 20 μm .

(B) Spindle microtubule dynamics parameters plotted over spindle length in the indicated cleavage stage or condition. Key for different stages and conditions indicated at the bottom of the graphs. (Control: red, *C27D9.1(RNAi)*: orange, *cls-2(RNAi)*: purple). Each dot represents a mean dynamics parameter over the corresponding spindle length measured in an individual blastomere. ($n(\text{cells}) \geq 10$ with $n(\text{events/cell}) \geq 60$). Pearson correlation coefficient (r^2) for the control condition indicated at the top of each graph if $p \leq 0.01$ (no corr. is indicated otherwise).

(C) Same as (B) for astral microtubules. (Control: green, *C27D9.1(RNAi)*: blue, *cls-2(RNAi)*: pink).

(D) Average theoretical microtubule length $\langle L \rangle$ plotted over experimentally measured average spindle length in the indicated conditions (Control: red, *C27D9.1(RNAi)*: orange, *cls-2(RNAi)*:

purple). $\langle L \rangle = \frac{Vg \times Vs}{Vs \times fc - Vg \times fr}$ with Vg : Growth rate, Vs : Shrinkage rate, fc : Catastrophe frequency, fr : Rescue frequency. Dotted red line and black lines represent the linear regression and 95% confidence interval respectively.

Figure 4. Spindle Length Scales with Cell Volume and Microtubule Growth Rate During Embryo Cleavage in the Sea Urchin *P. lividus*

(A) (Top) Schematic representations of early embryonic divisions of the sea urchin *Paracentrotus lividus*. Top views schematized for the 2- and 4-cell stages. All other schemes represent side views with the animal pole at the bottom. At the 16-cell stage, micromeres highlighted in orange. (Bottom) Still frames from confocal live imaging of *P. lividus* embryos microinjected with ATTO 565-labelled pig brain tubulin during the first six embryonic divisions (1- to >44-64-cell stage). Scale bar, 20 μm .

(B) Microtubule dynamics parameters for spindle microtubules plotted at each cleavage stage (1- to >44-64-cell stage). Each dot corresponds to an individual microtubule. Microtubule growth rate significantly varies between stages (one-way ANOVA with Tukey's multiple comparison tests: $p < 0.0001$), except between the 16-cell micromeres, the 32-cell and the >44-64-cell macromeres ($p > 0.5$ in all cases). However, the 16-cell micromeres and the 32-cell macromeres, as well as the 32-cell and the >44-64-cell macromeres differ significantly using a Student t-test ($p = 0.0004$ and 0.0039 respectively), but not the 16-cell micromeres compared to the >44-64-cell macromeres ($p = 0.85$). All parameters including sample size, mean and SD are listed in Table S2. (Horizontal bars, means; error bars, SD; $n(\text{cells}/\text{stage}) \geq 5$, $n(\text{microtubules}/\text{stage}) \geq 55$).

(C) Mean growth rate for spindle microtubules plotted at each cleavage stage (1- to >44-64-cell stage) over the average corresponding cell volume. (Error bars, SD).

(D) Mean spindle length plotted at each stage (1- to >44-64-cell stage) over the corresponding average spindle microtubule growth rate. Dotted blue line and black lines represent the linear regression and 95% confidence interval respectively. Pearson correlation coefficient (r^2) is indicated at the top of the graph because $p \leq 0.01$. (Error bars, SD).

Figure 5. Microtubule Growth Rate Scales Spindle Length in Computational 3D Spindle Models

(A) Spindle length scaling with microtubule growth rate and cell volume. Astral and spindle microtubules and a cell boundary are included in these simulations. Images correspond to steady state spindles obtained after running the simulations for 200 s. The input growth rate indicated at the bottom left of each image. Scale bar, 5 μm .

(B) Simulated spindle length plotted over time at various microtubule growth rates. Color-coding of the growth rate indicated at the top, from magenta (0.39 $\mu\text{m/s}$) to red (0.17 $\mu\text{m/s}$).

(C) Simulated steady state (200 s) spindle length plotted over the effective average spindle microtubule growth rate. Growth rate color-coded as in (B). Experimental data in grey.

(D) Spindle length scaling with microtubule growth rate. Only spindle microtubules are included in these simulations. Images correspond to a spindle obtained with a microtubule growth rate of 0.31 $\mu\text{m/s}$ at the beginning of the simulation (0 s, top) and after running the simulation for 100 s (middle) and 190 s (bottom). Scale bar, 5 μm .

(E) Simulated spindle length plotted over time at various effective average spindle microtubule growth rates. Color-coding of growth rate indicated at the top, from magenta (0.42 $\mu\text{m/s}$) to red (0.15 $\mu\text{m/s}$).

(F) Simulated steady state (200 s) spindle length plotted over spindle microtubule growth rate. Growth rate color-coded as in (E). Experimental data in grey.

Figure 6. Spindle Assembly Rate Scales with Spindle Microtubule Growth Rate During *C. elegans* Embryo Cleavage

(A) Left: Schematics of the spindle assembly process in the *C. elegans* embryo from NEBD (top) to anaphase onset (bottom). Right: Still frames from live confocal imaging of *C. elegans* embryos co-expressing mCherry-tagged Histone H2B (Magenta) and GFP-tagged β -tubulin (Grey) during spindle assembly in the first six embryonic divisions (1- to 32-cell stage from left to right). Timings are relative to NEBD. Images correspond to maximum projections of z-stacks. Scale bar, 10 μm .

(B) Spindle assembly timing measured from the 1- to the 32-cell stage in *C. elegans* embryos and plotted over the corresponding spindle length at anaphase onset. Each dot corresponds to an individual spindle. ($n \geq 9$ per stage).

(C) Mean spindle assembly rate (Spindle length/Spindle assembly timing) measured at each cleavage stage from the 1- to the 16-cell stage plotted over the corresponding average spindle microtubule growth rate. Dotted grey line represents the linear regression.

(D) Mean spindle assembly rate (Spindle length/Spindle assembly timing) measured at each cleavage stage from the 1- to the 16-cell stage plotted over the corresponding average spindle length. Dotted grey line represents the linear regression.

SUPPLEMENTARY FIGURE LEGENDS

Figure S1. Allometric Relationship Between Spindle Length and Cell Volume in the *C. elegans* Embryo. Related to Figure 1

(A) Still frames from live 2-photon imaging of *C. elegans* embryos expressing a GFP-tagged plasma membrane probe (Pleckstrin Homology (PH) domain) during the first five embryonic divisions (1- to 16-cell stage). Images correspond to maximal projections of z-stacks covering the entire thickness of the embryo. Scale bar, 20 μm .

(B) 3D surface reconstructions from live 2-photon imaging of *C. elegans* embryos expressing a GFP-tagged plasma membrane probe (PH domain) during the first five embryonic divisions (1- to 16-cell stage). Blastomere names are indicated except for the 16-cell stage. At the 8-cell stage, progeny of AB and P1 were grouped together as ABxx and P1xx respectively.

(C) Spindle length at anaphase onset in the different blastomeres during the first five embryonic divisions (1- to 16-cell stage). Each dot corresponds to an individual spindle. (Horizontal bars, means; error bars, SD; $n \geq 6$ per type of blastomere).

(D) Cell volume of the different blastomeres during the first five embryonic divisions (1- to 16-cell stage). Each dot corresponds to an individual blastomere. (Horizontal bars, means; error bars, SD; $n \geq 6$ per type of blastomere).

(E) Average spindle length plotted over the average cell volume for the different blastomeres. (Error bars, SD).

(F) Mean spindle length plotted over the cube root of the average cell volume on a \log_2 - \log_2 scale for the different blastomeres indicated on the left. (Error bars, SD).

Figure S2. Fluorescent Protein Tags and/or Promoter Used to Drive β -tubulin Expression do not Affect Microtubule Dynamics in the *C. elegans* Embryo. Related to Figure 1 and 2

(A) Mean astral microtubule growth rate plotted over the average cell volume at each cleavage stage (1- to 16-cell stage) for the different worm strains indicated on the right. Astral microtubule growth rate was measured in three different worm strains during early embryonic development from the 1- to the 16-cell stage. Microtubule growth rate was tracked using GFP-tagged β -

tubulin expressed under two different embryonic promoters (*mex-5* or *pie-1*) or using mCherry-tagged β -tubulin (under the *pie-1* promoter). ($n \geq 6$ per type of blastomere; Error bars, SD).

(B) Formulas used for the calculation of J and $\langle L \rangle$ from (Verde et al., 1992).

(C) Average theoretical microtubule length $\langle L \rangle$ calculated using the formula in (B) and plotted over the experimentally measured average spindle length in the indicated conditions (GFP-tagged β -tubulin under *mex-5*: red, mCherry-tagged β -tubulin under *pie-1*: purple). Since microtubules were in a bounded state ($J < 0$) under all conditions, $\langle L \rangle$ could be calculated. Dotted red and black lines are the linear regression curve and 95% confidence interval respectively for the GFP-tagged β -tubulin under the *mex-5* promoter (red) used in main Figures 1 to 4.

Figure S3. Mitotic Spindles Reach a Steady-State Length Before Anaphase Onset in *C. elegans* Cleaving Embryos. Related to Figure 1 and 2

(A) Kymographs extracted from confocal live imaging of *C. elegans* embryos expressing GFP-tagged β -tubulin during the first embryonic division (1-cell stage) treated with DMSO (control, top) or with 20 μ M of the proteasome inhibitor Clasto-Lactacystin β -Lactone (CL β L diluted in DMSO, bottom) to inhibit the metaphase-to-anaphase transition. Spindles poles (black arrowheads) are visible as two dark stripes that separate during anaphase in controls and stay at the same distance over time in CL β L-treated embryos. Timings relative to NEBD monitored by diffusion of free GFP-tagged β -tubulin in the nuclear area. Horizontal scale bar, 50s; Vertical scale bar, 5 μ m

(B) Spindle length (aster-to-aster distance) plotted over time in DMSO (colors) and CL β L (grey) treated embryos at each cleavage stage (1- to 16-cell stage). Timings relative to NEBD. ($n \geq 5$ spindles per stage in each condition; error bars, SD).

Figure S4. Allometric Relationship Between Spindle Length/Width and Cell Volume in the *P. lividus* Embryo. Related to Figure 4

(A) Mean spindle length in *P. lividus* measured at anaphase onset and plotted over the cube root of the average cell volume for the different blastomeres on a \log_2 - \log_2 scale. (Error bars, SD; $n \geq 5$ per stage).

(B) Mean spindle length (blue) and width (pink) (left Y-axis) and centrosome radius (green) (right Y-axis) plotted over the corresponding average cell volume for the different stages. (Error bars, SD). A schematic representation of the spindle shape change observed between large and small cells in *P. lividus* embryos shown on the right.

Figure S5. Microtubule Dynamics and Spindle Assembly Timing in the Computational 3D Simulations. Related to Figure 5

(A) Simulated effective growth rate of spindle microtubules growing freely in the cytoplasm (triangles), captured at metaphase plate (squares) or the average of both populations (plain circles) plotted over the input growth rate. Color-coding of the input growth rate indicated at the bottom, from magenta (0.42 $\mu\text{m/s}$) to dark red (0.15 $\mu\text{m/s}$). See Table S3 and Methods for more details.

(B) Simulated effective growth rate of astral (triangles) and spindle (squares) microtubules plotted over the input growth rate. Color-coding of the input growth rate indicated at the bottom, from magenta (0.39 $\mu\text{m/s}$) to dark red (0.17 $\mu\text{m/s}$).

(C) Simulated average astral (triangles) and spindle (squares) microtubule lengths plotted over the input growth rate. Color-coding is the same as in (B).

(D) Spindle assembly timing is independent of the input microtubule growth rate in the computational 3D simulations. (Left) Simulated spindle length plotted over time at various microtubule growth rates for the simulation shown in Figure 5A. Color-coding of the growth rate indicated at the bottom, from magenta (0.39 $\mu\text{m/s}$) to red (0.17 $\mu\text{m/s}$). (Center) Example of curve fitting for one input growth rate (0.39 $\mu\text{m/s}$). *In silico* data fitted to single exponential functions $f(t) = (a - b)(1 - e^{-\frac{t}{\tau}}) + b$, where ‘a’ corresponds to the plateau, ‘b’ to the initial spindle length and ‘ τ ’ to the time constant required to reach $\sim 63\%$ of the maximal amplitude ($1 - e^{-1}$ when $t = \tau$). (Right) The values of τ extracted for each input growth rate and plotted over the input growth rate.

Figure S6. Estimation of the Tubulin Concentration in Early *C. elegans* Embryos.

(A) Quantitative western-blot using an anti- α -tubulin antibody (DM1 α) on 1- to ~64-cell stage embryo extracts and on increasing amounts of purified pig brain tubulin.

(B) Embryo volume measured in Figure 1 was used to estimate the tubulin concentration. The amount of tubulin per embryo was estimated from the western-blot (A).

Figure S7. Comparison of Microtubule Dynamics and Spindle Lengths Between *P. lividus* and *C. elegans* Embryos. Related to Figure 1 and 4

(A) Growth rate for spindle microtubules in *P. lividus* and *C. elegans* (same as Figure 1C and 4B) plotted at each cleavage stage (1- to >44-64-cell stage in *P. lividus* and 1- to 16-cell stage in *C. elegans*). Each dot corresponds to an individual microtubule. Color-coding and symbols shown in the right boxes. (Horizontal bars, means; error bars, SD; $n(\text{cells}/\text{stage}) \geq 5$, $n(\text{microtubules}/\text{stage}) \geq 55$) in *P. lividus* ; $n(\text{cells}/\text{stage}) \geq 12$, $n(\text{microtubules}/\text{stage}) \geq 288$) in *C. elegans*. All parameters including sample size, mean and SD listed in Table S2.

(B) Mean growth rate for spindle microtubules plotted at each cleavage stage over the corresponding average spindle length. (Bars, SD).

(C) Mean growth rate for spindle microtubules plotted at each cleavage stage over the average corresponding cell volume. (Bars, SD).

(D) Mean spindle length plotted over the cube root of the average cell volume on a \log_2 - \log_2 scale. (Error bars, SD).

(E) Average theoretical microtubule length $\langle L \rangle$ plotted over the experimentally measured spindle length. (Error bars, SD).

(F) (Left) Average theoretical microtubule length $\langle L \rangle$ plotted over the average cell volume. (Right) Magnification of the graph for the smaller cells (volume < 125 pL). (Error bars, SD).

STAR METHODS

Detailed methods are provided in the online version of this paper and include the following:

- KEY RESOURCE TABLE
- CONTACT FOR REAGENT AND RESOURCE SHARING
- EXPERIMENTAL MODEL AND SUBJECT DETAILS
 - *Caenorhabditis elegans*
 - *Paracentrotus lividus*
- METHOD DETAILS
 - RNA-mediated interference (RNAi) and drug treatment in *C. elegans*
 - Estimation of the tubulin heterodimer concentration in the *C. elegans* embryo by quantitative western-blot
 - Tubulin preparation and fluorescent labeling
 - Two-photon live microscopy of *C. elegans* embryos
 - Spinning-disc live microscopy of *C. elegans* embryos
 - Injection and Imaging of sea urchin embryos
 - Image analysis
 - Analysis of microtubule dynamics
 - Cytosim simulations
- QUANTIFICATION AND STATISTICAL ANALYSIS
- DATA AND SOFTWARE AVAILABILITY
 - Cytosim

KEY RESOURCE TABLE

CONTACT FOR REAGENT AND RESOURCE SHARING

Further information and requests for resources and reagents should be directed to and will be fulfilled by the Lead Contact, Julien Dumont (julien.dumont@ijm.fr). Requests related to the simulations should also be addressed to Francois Nedelec (nedelec@embl.de).

EXPERIMENTAL MODEL AND SUBJECT DETAILS

Caenorhabditis elegans

C. elegans are small and transparent soil worms with rapid, invariant and perfectly described development (Sulston and Horvitz, 1977; Sulston et al., 1983). Spindle assembly has been extensively studied in *C. elegans* (Muller-Reichert et al., 2010), primarily because many key proteins and mechanisms are highly conserved with other metazoans. All *C. elegans* strains were maintained at 23°C or at 16°C for the *cyk-1^{formin(ts)}* mutant strain (JCC49 and JDU156) and cultured using standard procedures (Brenner, 1974). Different strains were obtained either by stable single insertion by MosSCI (Frokjaer-Jensen et al., 2008) or by crossing with pre-existing strains. *C. elegans* worm strains and genotypes are listed in the Key Resources Table.

Paracentrotus lividus

Paracentrotus lividus sea urchins were purchased from the Roscoff Marine Station (Station Biologique de Roscoff, CNRS-UPMC, France) and maintained in seawater at 16°C for several weeks before use.

METHOD DETAILS

RNA-mediated interference (RNAi) and drug treatment in *C. elegans*

Depletion of C27D9.1 was done by feeding as described by Kamath et al., (Kamath et al., 2001). For L1 larvae synchronization, adult worms were bleach-treated (1.2% NaOCl, 250 mM KOH in water; {Stiernagle, 2006 #85}) to release embryos. Embryos were allowed to hatch and left to starve in M9 buffer (22 mM KH₂PO₄, 42 mM Na₂HPO₄, 86 mM NaCl). Synchronized L1 hermaphrodite larvae were grown on regular NGM plates seeded with the OP50 bacterial strain for 44 hours (until they reached the adult stage), and then adult worms were transferred on RNAi feeding plates for at least 24 hours. RNAi feeding was performed on NGM plates containing 50 µg/ml ampicillin (Euromedex) and 1 mM IPTG (Isopropyl β-D-thiogalactopyranoside, Euromedex) and seeded with the HT115(DE3) bacterial strain transformed with the empty L4440 vector (control) or containing the C27D9.1 target sequence (corresponding to nt179-1366 of the genomic sequence). Depletion of CLS-2^{CLASP} (R107.6) was performed by microinjection of the corresponding dsRNA in L4 hermaphrodite larvae as previously described (Fire et al., 1998). The dsRNA targeting *cls-2^{CLASP}* was synthesized from a purified PCR product (corresponding to nt164-1081 of the genomic sequence, QIAquick PCR purification, Qiagen) that contained the T3 and T7 phage RNA polymerase promoter sequences (T3:

taatacgactcactatagg ; T7 : aattaaccctcactaaagg) in 5' and 3', respectively, using the MEGAscript T3 and T7 transcription kits (ThermoFischer Scientific). Single stranded RNAs were purified using the MEGAclean Transcription Clean-Up kit (ThermoFischer Scientific). Sense and antisense single stranded RNAs were mixed in equimolar concentrations and annealed at 68°C for 10 min followed by 37°C for 30 min. DsRNAs were aliquoted, snap-frozen in liquid nitrogen and stored at -80°C until use. The dsRNA targeting *cls-2^{CLASP}* was injected in L4 hermaphrodites at a concentration of 1.8 µg/µl. Partial depletion of CLS-2^{CLASP} was obtained 25 to 27 h post-injection at 23°C (Maton et al., 2015). PTR-2 (C32E8.8) depletion was performed in a humid chamber by soaking 25 to 30 L4 hermaphrodite larvae in a 5 µl drop of the corresponding dsRNAs (synthesized as previously and corresponding to nt1886-2904 of the genomic sequence) supplemented with 2.86 mM spermidine (Sigma) and 0.05 % gelatin (Sigma). L4 larvae were soaked at 20°C for 24 hours, then washed twice in M9 medium and transferred on NGM plates for another 24 hours at 20°C before observation. PTR-2-depleted embryos are defective in eggshell formation and are therefore permeable and amenable to drug treatments. To induce a metaphase arrest in zygotes, PTR-2-depleted adult worms were dissected in 20 µM clastolactacystine β-lactone (CLβL, Merck Millipore) in L-15 blastomere culture medium [0.5 mg/mL Inulin (Sigma); 25 mM HEPES pH 7.5; 3 mL Leibowitz L-15 Media and 20% (vol/vol) Heat-Inactivated FBS (Life Technologies)] with 1% DMSO (Euromedex) final concentration.

Estimation of the tubulin heterodimer concentration in the *C. elegans* embryo by quantitative western-blot

C. elegans early embryos (1- to ~64-cell stage) were extracted from synchronized adult N2 worms by bleaching as described earlier in the “RNA-mediated interference (RNAi) and drug treatment in *C. elegans*” method section. Embryos were then resuspended in M9 buffer. The number of embryos per volume and their approximate number of blastomeres (stage) were estimated under a dissection scope (Nikon). Embryos were then lysed into 1x Laemmli sample buffer (80 mM Tris-HCl pH 6.8, 140 mM 2-Mercaptoethanol, 2.5% SDS, 10% glycerol) by vortexing in presence of 0.7 mm diameter Zirconia beads (BioSpec Products) 3 times 5 min at 4°C with pauses of 5 min. Lysis efficiency was assessed using a dissection scope. Samples were then incubated 5 min at 95°C before loading on a SDS-PAGE gel. The equivalent of ~1120 or ~2240 embryos were loaded on a SDS-PAGE gel (10%, 37.5:1 acrylamide:bisacrylamide)

together with increasing amounts of porcine brain tubulin purified as described in “Tubulin preparation and fluorescent labeling” (Figure S6). *C. elegans* and porcine brain tubulin samples were treated similarly. Proteins were transferred onto a nitrocellulose blotting membrane Protran 0.45 μm (Amersham, GE Healthcare) by liquid transfer. Membrane was incubated with DM1 α antibody (Sigma) diluted 1/1000 in 5% fat-free milk in Tris-buffered saline (TBS: 50 mM Tris pH 7.5, 150 mM NaCl). Protein bands were revealed with an HRP-labeled goat anti-mouse IgG 1:10,000 (GE Healthcare) and chemoluminescence (ECL SuperSignal West Pico, ThermoScientific). Detection was performed on a luminescence image analyzer LAS-4000 (Fujifilm). Band intensities were analyzed using ImageJ. The amount of α -tubulin contained per embryo was estimated to be between 2.04 and 2.73×10^{-11} g. This amount corresponds to a concentration of 0.93 to 1.24 g/L (Embryo volume = 2.2×10^{-11} L, Figure S1 and Table S1) or 18.6 and 24.8 μM (molecular weight of α -tubulin = 50,000 g/mol). *C. elegans* microtubules are composed of 11 protofilaments on average (Chalfie and Thomson, 1982), and tubulin heterodimers are 8 nm long (Nogales et al., 1998). If we assume an average tubulin heterodimer concentration of 22 μM , a *C. elegans* embryo contains enough tubulin heterodimers to build 21.2 cm of microtubules in total. The metaphase spindle in the 1-celled zygote is composed of around $\sim 20,000$ microtubules, which are on average 4 μm long (Redemann et al., 2017). This average microtubule length also corresponds to the theoretical average microtubule length $\langle L \rangle$ calculated from the dynamics parameters in the 1-celled zygote (Table S1). Therefore, in the 1-celled zygote in metaphase, spindle microtubules reach a total length of about 8 cm ($20,000 \times 4 \mu\text{m}$). We thus concluded that the *C. elegans* zygote contains enough tubulin heterodimers to build between 2 and 3 mitotic spindles.

Tubulin preparation and fluorescent labeling

Tubulin was obtained from pig brains following cycles of polymerization and depolymerization (Castoldi and Popov, 2003). Tubulin was then labeled with NHS-ester-ATTO 565 (ATTO-TEC) and further purified through two polymerization/depolymerization cycles (Hyman, 1991).

Two-photon live microscopy of *C. elegans* embryos

Embryo and blastomere volume measurements were made from Z-stacks of 1- to 16-cell stage embryos expressing a GFP-tagged membrane marker (OD58 strain that expresses the GFP-PH-

domain under a *pie-1* germline promoter). Gravid worms were dissected in a 5 μ l drop of egg salt buffer (ESB, 25 mM HEPES pH 7.3, 118 mM NaCl, 48 mM KCl, 2 mM CaCl₂, 2 mM MgCl₂). Embryos were then transferred between two 3% agarose pads to prevent compression and to minimize refractive index mismatch. The montage was then placed on a glass slide, sealed with paraffin. A well of Valap (petroleum jelly:lanolin:paraffin, 1:1:1) was made around it and filled with water for imaging in immersive conditions. An upright two-photon microscope with a Zeiss Plan APO 20x/NA1.0 water objective was used (Lavision Biotec). GFP was excited with a pulsed laser at 920 nm. Emission at 535 nm was collected with a GaAsP detector (Lavision Biotec). The entire embryo was imaged with 1 μ m Z-sectioning and 190 nm lateral sampling.

Spinning-disc live microscopy of *C. elegans* embryos

Gravid worms were dissected in egg salt buffer (ESB, see above). Embryos were transferred on a 3% agarose pad between a glass slide and a coverslip. The montage was then sealed with Valap. Live imaging was done using a spinning-disk (CSU-X1, Yokogawa) confocal microscope (Roper Scientific) coupled to a CoolSnap HQ2 CCD camera (Photometrics) and all acquisition parameters were controlled by MetaMorph 7 software (Molecular Devices). For microtubule dynamics parameter extraction, images were acquired on a single channel (491 nm excitation) every 0.5 sec with a single z-plan using a Nikon CFI APO LBDA S 60x/NA1.4 oil objective with no binning. To measure spindle assembly timings, images were acquired on two channels sequentially (491 and 561 nm excitations) every 5 sec with 11 z-plan at 1 μ m intervals using a Nikon CFI APO LBDA S 40x/NA1.25 water objective with no binning. Maximal projections are presented.

Injection and Imaging of sea urchin embryos

Gametes were collected by intracoelemic injection of 0.5M KCl. Eggs were washed several times in fresh seawater, kept at 12-14°C and used within 24h. Sperm were kept concentrated for several days at 4°C. Upon use, the sperm suspension was diluted 1000 times in fresh seawater and activated by vigorous aeration. Freshly collected *P. lividus* eggs were dejellied by pouring through a 80 μ m pore Nitex mesh (Sefar). Dejellied eggs were immobilized on a protamine (Sigma) treated 60 mm diameter glass-bottom dish for both microinjection and imaging. Eggs were fertilized 20 min after ATTO 565-tubulin microinjection (2 mg/ml) by adding a few drops

of activated sperm. Live imaging was done using a spinning disk (CSU-W1, Yokogawa) confocal microscope (Leica Microsystems) coupled to an ORCA-Flash4.0 V2 CMOS camera (Hamamatsu). All acquisition parameters were controlled by MetaMorph 7 software (Molecular Devices). Images were acquired on a single channel (561 nm excitation) every 1 sec with a single z-plan using a Leica Plan APO 63×/NA1.2 water objective.

Image analysis

Two-photon acquisitions of GFP-PH (membrane marker) during *C. elegans* embryonic development were analyzed using Imaris software (Bitplane). *C. elegans* blastomere volumes were extracted after semi-automated surface reconstruction. *P. lividus* blastomere volumes were estimated from experimentally measured blastomere diameters. Spinning-disk confocal images were analyzed using the Fiji package (<http://fiji.sc/>; <https://imagej.nih.gov/ij/>). Spindle length was estimated as the aster-to-aster distance (Crowder et al., 2015) on GFP-tubulin images. Metaphase plate thickness and centrosome radius were measured on segmented mCherry-histone and GFP- β -tubulin images in *C. elegans* embryos or ATTO 565-tubulin images in *P. lividus* embryos. At each cleavage stage in *C. elegans* embryos, a 10% or 40% grey level threshold were applied on mCherry-histone or GFP- β -tubulin images respectively. In *P. lividus* embryos, a 30% grey level threshold was applied on ATTO 565-tubulin images for centrosome radius measurements. These thresholds were selected to obtain the sharpest limit between the metaphase plate histone signal or the centrosome and the cytoplasmic background with minimal erosion of the signal. Measured values were used in Cytosim simulations to build *in silico* spindle 3D models.

Analysis of microtubule dynamics

Individual embryos were imaged at a single stage of cleavage and for less than 10 min to avoid phototoxicity-induced bias (Lacroix and Maddox, 2014; Lacroix et al., 2016). Kymographs were traced from time-lapse sequences using the 'Multi kymograph' plugin (http://imagej.net/Multi_Kymograph) in Fiji. Polymerization and depolymerization rates, as well as catastrophe and rescue frequencies, were extracted from these kymographs by manual tracking and semi-automated parameter extraction using homemade macros in Fiji and Excel (Microsoft) software. Catastrophe and rescue frequencies were defined as the inverse of the

average growth time or shrinkage time, respectively {Desai, 1997 #92;Komarova, 2002 #93;Walker, 1988 #58}. Although this method could potentially overestimate catastrophe and rescue occurrences (which would be identical in all tested experimental conditions), it allows estimating both parameters independent of microtubule pausing, moving out-of-focus during live imaging or entering in the fluorescence-saturated centrosome area.

Cytosim simulations

All simulations were performed in 3D using Cytosim (www.cytosim.org, (Nedelec F, 2007)). Cytosim simulations have already been used to show how polymerization forces and thus microtubules dynamics could affect centrosome positioning (Letort et al., 2016). Following this approach, we aimed for a minimal model in which spindle length, corresponding to the distance between two asters, would be influenced by microtubules dynamic behavior. A detailed list of Cytosim parameters for each object in the simulations is presented in Table S3. Spindle poles were modeled using microtubules radiating radially from a sphere (asters). The surface of the sphere contains a preset number of nucleation sites, at which microtubules are anchored at their minus-ends constraining their position and orientation. The minus-ends are static, while the plus-ends may grow or shrink, stochastically switching between these states following the usual phenomenological model of dynamic instability. The metaphase plate was represented as a fixed and rigid disc positioned orthogonally at the center of the “cell”. Although microtubules were excluded from inside this plate, microtubule-associated molecules (called “singles”, each made of one “hand”) anchored on this disc and capable of tracking growing microtubule ends were used to mimic the chromokinesins present on chromosomes, as well as the capture of microtubules by pro-metaphase kinetochores. The primary function of these microtubule-associated molecules is to prevent microtubules from sliding on the surface of the “metaphase plate”. At the start of every simulation, the two asters were positioned symmetrically 2 μm away from the “metaphase plate” on each side.

The input growth rate (v_0) varied within the range of experimental measurements made in *C. elegans* embryos from 1- to 16-cell stage. The effective microtubule growth rate was set to decrease exponentially under an opposing force as $v_g = v_0 e^{\frac{-F}{F_s}}$, where v_0 is the input growth rate and F_s is the force at which microtubule polymerization stalls (Dogterom and Yurke, 1997). Consequently, microtubules encountering the metaphase plate grew dramatically slower, in

agreement with *in vivo* measurements at the kinetochore (Maddox et al., 2003; Tirnauer et al., 2002). Further, in the first simulation that contained both astral and spindle microtubules, a force-dependent increase in the catastrophe rate $k_{cat} = \frac{k_{cat}^{stall}}{1 + (k_{cat}^{stall}/k_{cat}^0 - 1)v_g/v_0}$ (see also Table S3) induced microtubule shrinking soon after cortical or metaphase plate contact. This force-dependent microtubule shrinking was not implemented in the second simulation (with only spindle microtubules). So, the effective average growth rate of microtubules in our simulations represented the mean rate of free growing microtubules and stalled microtubules at the metaphase plate (or at the cortex) (Figure S5A).

Two different spindle models were tested, as described below. (Figure 5A-C): This model included 500 microtubules per aster. 400 microtubules were allowed to grow uniformly in space, and 100 microtubules per aster were constrained in a cone directed toward the metaphase plate to mimic the higher microtubule density observed *in vivo* in the spindles of *C. elegans* embryos. *C. elegans* blastomeres were represented by 3D ellipsoids. Cell volume, metaphase plate thickness and radius were scaled together with respect to the input microtubule growth rate using realistic values extrapolated from our experimental measurements (TableS2B). Scaling to the input growth rate was done assuming a linear proportionality between microtubule growth rate and other dimensions. Due to their initial proximity to the metaphase plate, spindle microtubules were more likely to be stalled and therefore displayed a lower effective average growth rate than astral microtubules (Figure S5B). This was particularly true for higher initial rates and was reminiscent of the difference in the growth rates we measured *in vivo* between astral and spindle microtubules. This mild difference in the astral and spindle effective growth rates was sufficient to induce a significant deviation of the average microtubule length reached by the two populations (Figure S5C). The average length difference was not evident at low initial growth rates but was particularly clear for rates above 0.3 $\mu\text{m}/\text{sec}$. This result is in agreement with the evolution of $\langle L \rangle$ for astral and spindle microtubules calculated from *in vivo* measured parameters, which became closer between the two types of microtubules as cells get smaller (Table S1). The faster decrease of the average length of astral compared to spindle microtubules is likely due to increasing cortical surface to cell volume ratio as cleavage progresses. Indeed, the cortical surface decreases slower than the cell volume, so that astral microtubules are more likely to encounter the cortex and shrink, as blastomeres get smaller. Our simulation therefore

accurately recapitulates two key features of the dynamic behavior of astral and spindle microtubules *in vivo* during embryonic cleavage: 1) spindle microtubules grow slower and are, on average, shorter than astral microtubules during early cleavages and 2) these differences tend to fade as blastomeres become smaller (Figure S5B,C).

(Figure 5D-F): 50 microtubules were constrained in a spindle-shaped cone to reflect the *C. elegans* embryo spindle geometry (Table S2). Importantly, increasing or decreasing the number of microtubules had no effect on the final outcome of the simulations (data not shown). The two asters do not include astral microtubules and grow in an infinite space without a cell boundary.

QUANTIFICATION AND STATISTICAL ANALYSIS

All graphs were made in Prism 6 (GraphPad Software). Statistical analyses, including Student t-tests, one-way ANOVA multiple comparisons, linear regressions and Pearson and Spearman correlation tests were performed in Prism 6 (GraphPad software). Microtubule dynamics parameters have different variances, so we used the unequal variance unpaired t-test with the Welch's correction for normally distributed populations with unequal standard deviation. Tukey or Dunnett tests were performed for multiple comparisons following one-way ANOVA. In Figure 4B, multiplicity adjusted *p* value was estimated for the multiple comparison Tukey's test.

DATA AND SOFTWARE AVAILABILITY

Data availability

All data presented in this manuscript are available upon request to the lead author (julien.dumont@ijm.fr).

TABLE FOR AUTHOR TO COMPLETE

Please upload the completed table as a separate document. **Please do not add subheadings to the Key Resources Table.** If you wish to make an entry that does not fall into one of the subheadings below, please contact your handling editor.

KEY RESOURCES TABLE

REAGENT or RESOURCE	SOURCE	IDENTIFIER
Antibodies		
DM1 α anti-tubulin	Sigma-Aldrich	T9026
Bacterial and Virus Strains		
OP50 E. coli	Caenorhabditis Genetics Center (CGC)	http://www.cgc.cbs.umn.edu/strain.php?id=11078
HT115(DE3) E. coli	Caenorhabditis Genetics Center (CGC)	http://www.cgc.cbs.umn.edu/strain.php?id=8854
Biological Samples		
Chemicals, Peptides, and Recombinant Proteins		

ATTO-565 NHS-ester	ATTO-TEC GmbH	AD 565-35
Protamine sulfate	Sigma-Aldrich	P4020
<i>clasto</i> -Lactacystin β -Lactone (proteasome inhibitor)	Merck Millipore	426102
Critical Commercial Assays		
Deposited Data		
Experimental Models: Cell Lines		
Experimental Models: Organisms/Strains		
Nematode <i>Caenorhabditis elegans</i> , strain JDU19: [<i>mosl_5'mex-5_GFP::tbb-2</i> ; <i>mCherry::his-11</i> ; <i>cb-unc-119(+)</i>] I; <i>unc-119(ed3)</i> III	Julien Dumont lab, CNRS Institut Jacques Monod, Paris	N/A

Nematode <i>Caenorhabditis elegans</i> , strain JA1559: [pJA138; 5'pie-1::mCherry::tbb-2::3'pie-1]	Julie Ahringer lab	N/A
Nematode <i>Caenorhabditis elegans</i> , strain MDX20: unc-119(ed3). oJls1[unc-119(+) pie-1::GFP::tbb-2]	Maddox lab, University of North Carolina in Chapel Hill	N/A
Nematode <i>Caenorhabditis elegans</i> , strain JDU156: ijmSi7 [pJD348/pSW077; mosI_5'mex-5_GFP::tbb-2; mCherry::his-11; cb-unc-119(+)] I; cyk-1(or596ts) III; unc-119(ed3) III	Julien Dumont lab	N/A
Nematode <i>Caenorhabditis elegans</i> , strain JCC49: cyk-1(or596ts) III; ltlS37[pAA64; pie-1/mCHERRY::his- 58; unc-119 (+)] IV	Julie C. Canman lab	N/A
Nematode <i>Caenorhabditis elegans</i> , strain OD58: unc-119(ed3) III; ltlS38[pAA1; pie- 1::GFP::PH(PLC1delta1); unc-119 (+)]	Oegema & Desai lab	N/A
Nematode <i>Caenorhabditis elegans</i> , wild-type isolate (Bristol)	Caenorhabditis Genetics Center (CGC)	N2
Sea urchin <i>Paracentrotus lividus</i>	Station Biologique de Roscoff, France www.sb-roscoff.fr/fr	N/A
Oligonucleotides		
Forward primer for production of dsRNA targeting <i>cls-2</i> R107.6: TAATACGACTCACTATAGGttcaaggaaaagttggacc (Uppercase: T3 sequence)	(Maton et al., 2015)	N/A
Reverse primer for production of dsRNA targeting <i>cls-2</i> R107.6: AATTAACCCTCACTAAAGGggtgcatttctgattccacc (Uppercase: T7 sequence)	(Maton et al., 2015)	N/A
Forward primer for production of dsRNA targeting <i>ptr-2</i> C32E8.8: TAATACGACTCACTATAGGgtgcccgatcattctgcat (Uppercase: T3 sequence)	This study	N/A

Reverse primer for production of dsRNA targeting ptr-2 C32E8.8: AATTAACCCTCACTAAAGGgtggccatccaagagctgat (Uppercase: T7 sequence)	This study	N/A
Forward primer for production of dsRNA against C27D9.1 using L4440 feeding vector in HT115 bacteria: tcagcaaccagcacattctc	https://www.sourcebioscience.com/products/life-science-research/clones/rnai-resources/c-elegans-rnai-collection-ahringer/	SourceBioscience Location II-4A13
Reverse primer for production of dsRNA against C27D9.1 using L4440 feeding vector in HT115 bacteria: aaaatacgcttgacgttggc	https://www.sourcebioscience.com/products/life-science-research/clones/rnai-resources/c-elegans-rnai-collection-ahringer/	SourceBioscience Location II-4A13
Recombinant DNA		
Software and Algorithms		
ImageJ	NIH	https://imagej.nih.gov/ij/index.html
MATLAB	MathWorks	https://www.mathworks.com/products/matlab.html
GraphPad PRISM 6.0	GraphPad	https://www.graphpad.com/
Imaris	Bitplane	http://www.bitplane.com/imaris/imaris

Cytosim	Nédélec Laboratory	http://github.com/nedelec/cytosim
Other		

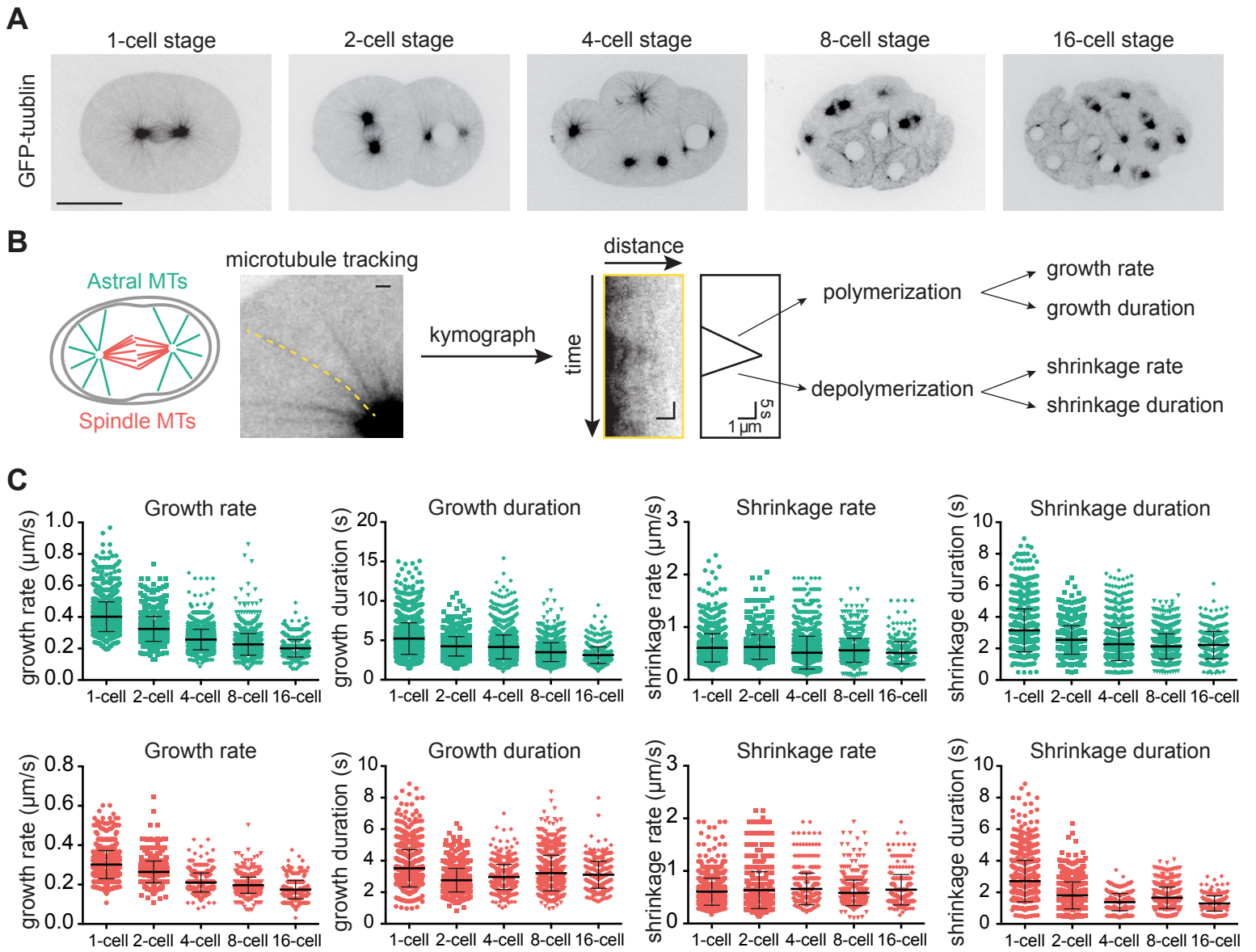
Figure 1

Figure 2

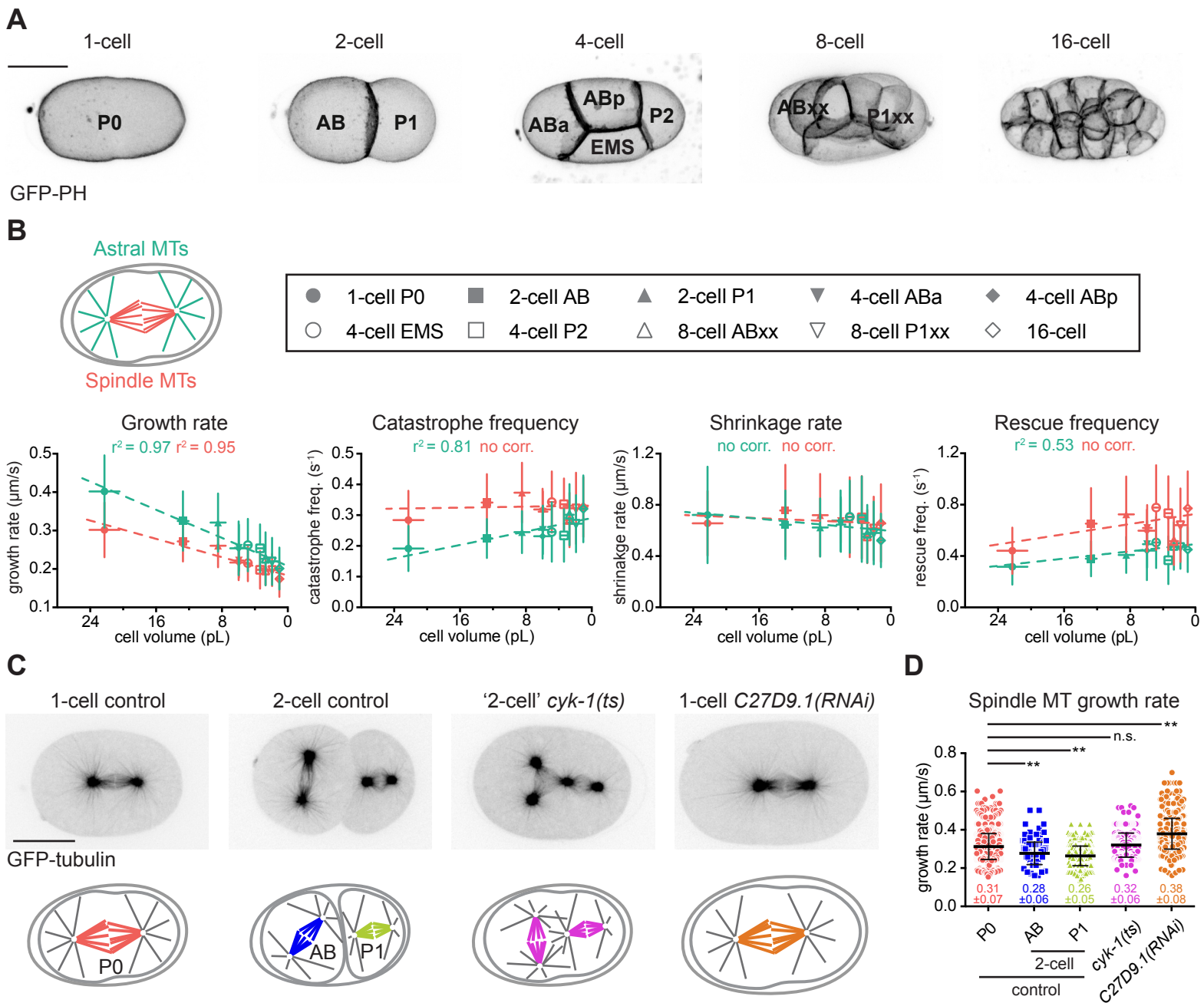


Figure 3

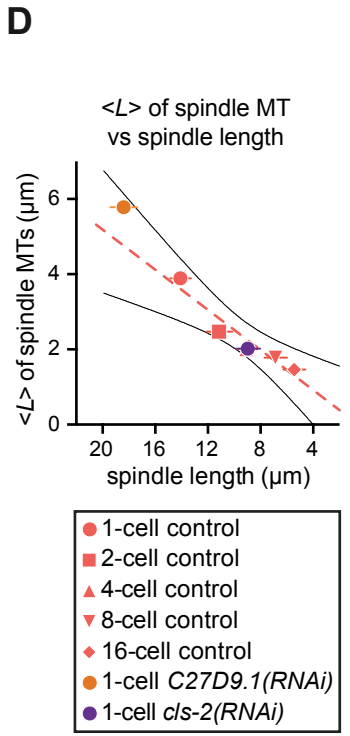
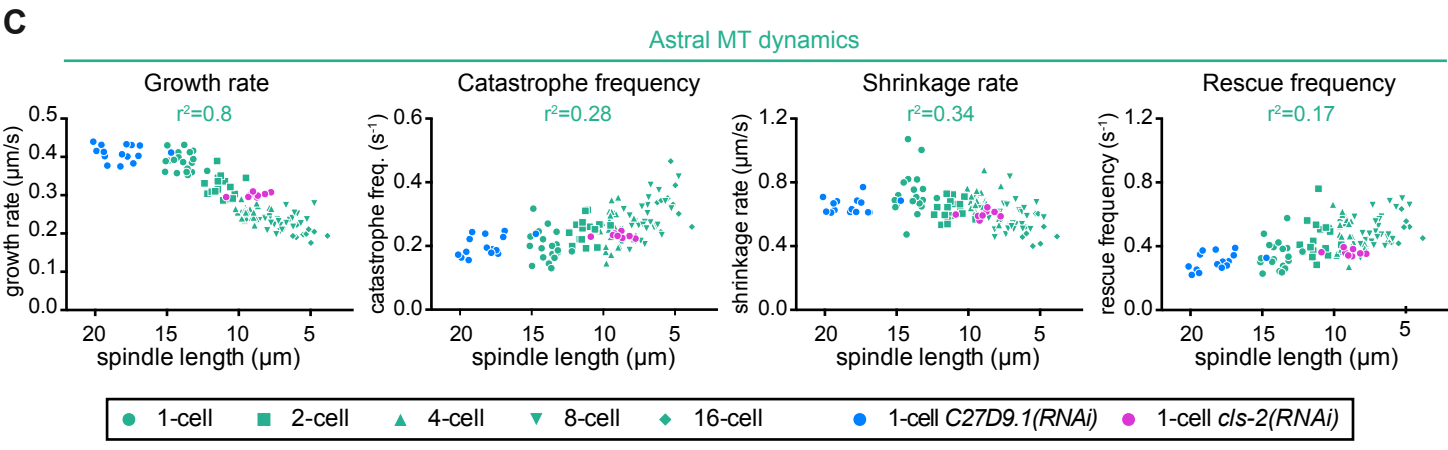
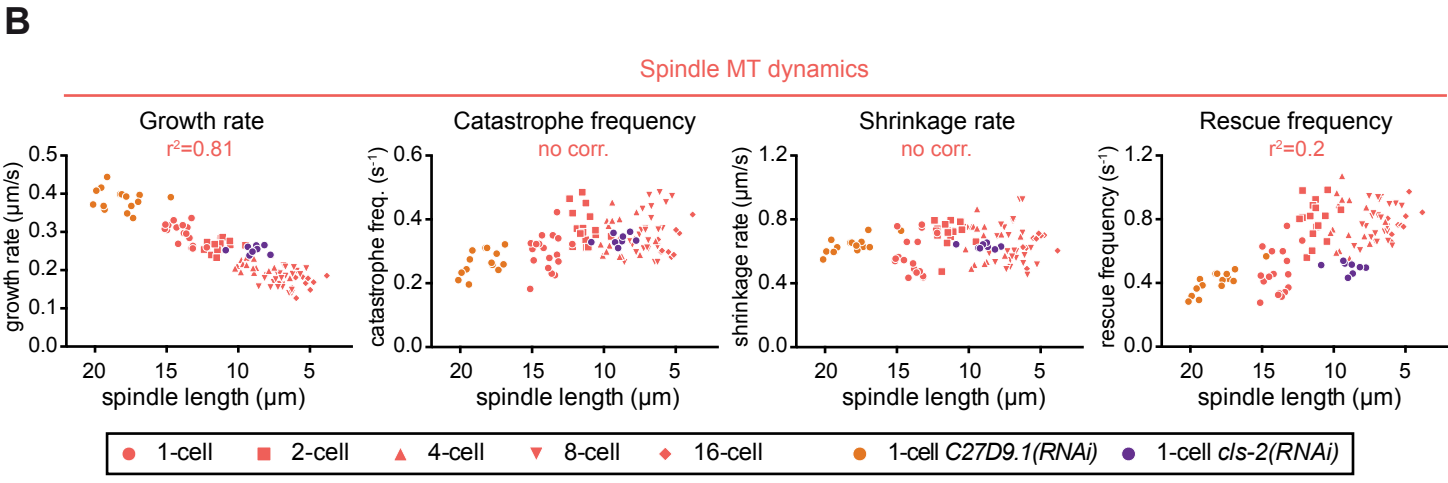
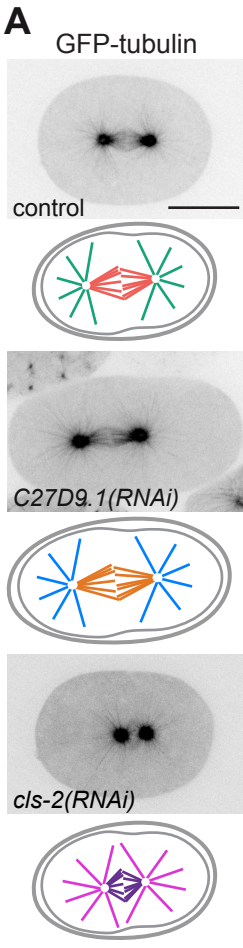
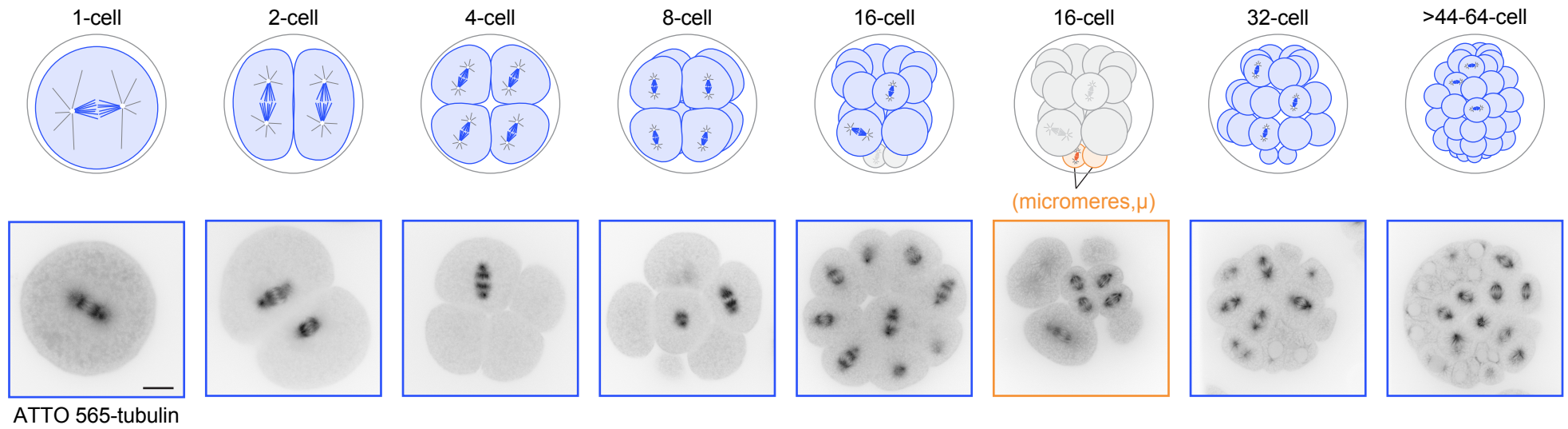


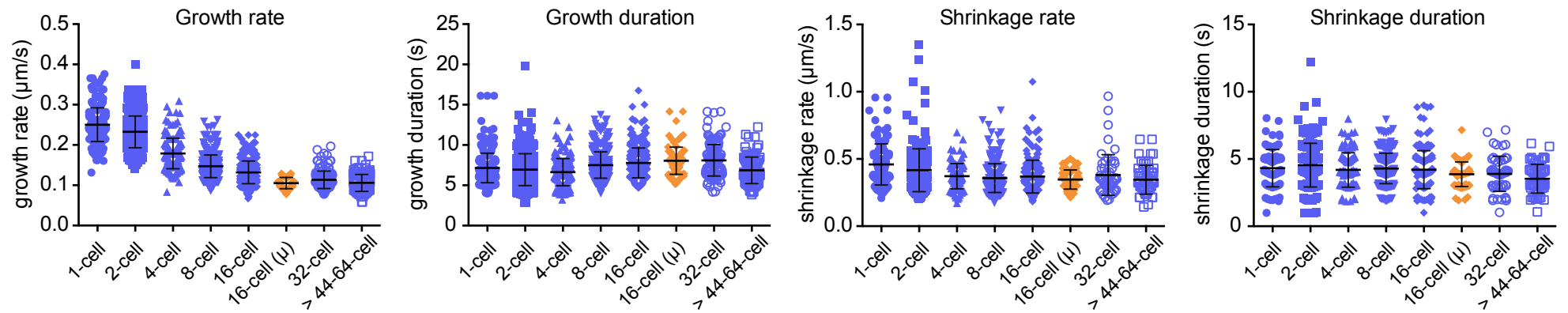
Figure 4

A

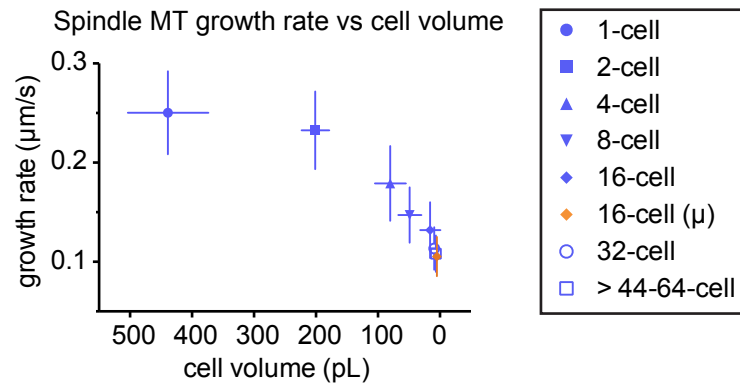
Early divisions in the sea urchin *Paracentrotus lividus*



B



C



D

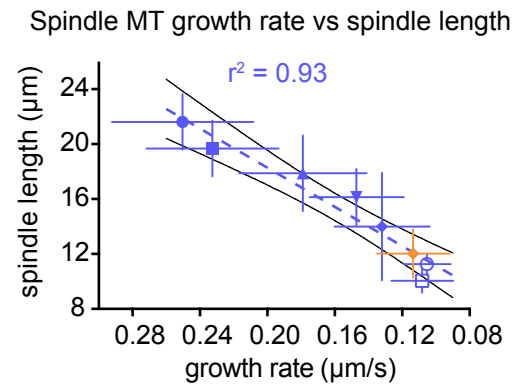


Figure 5

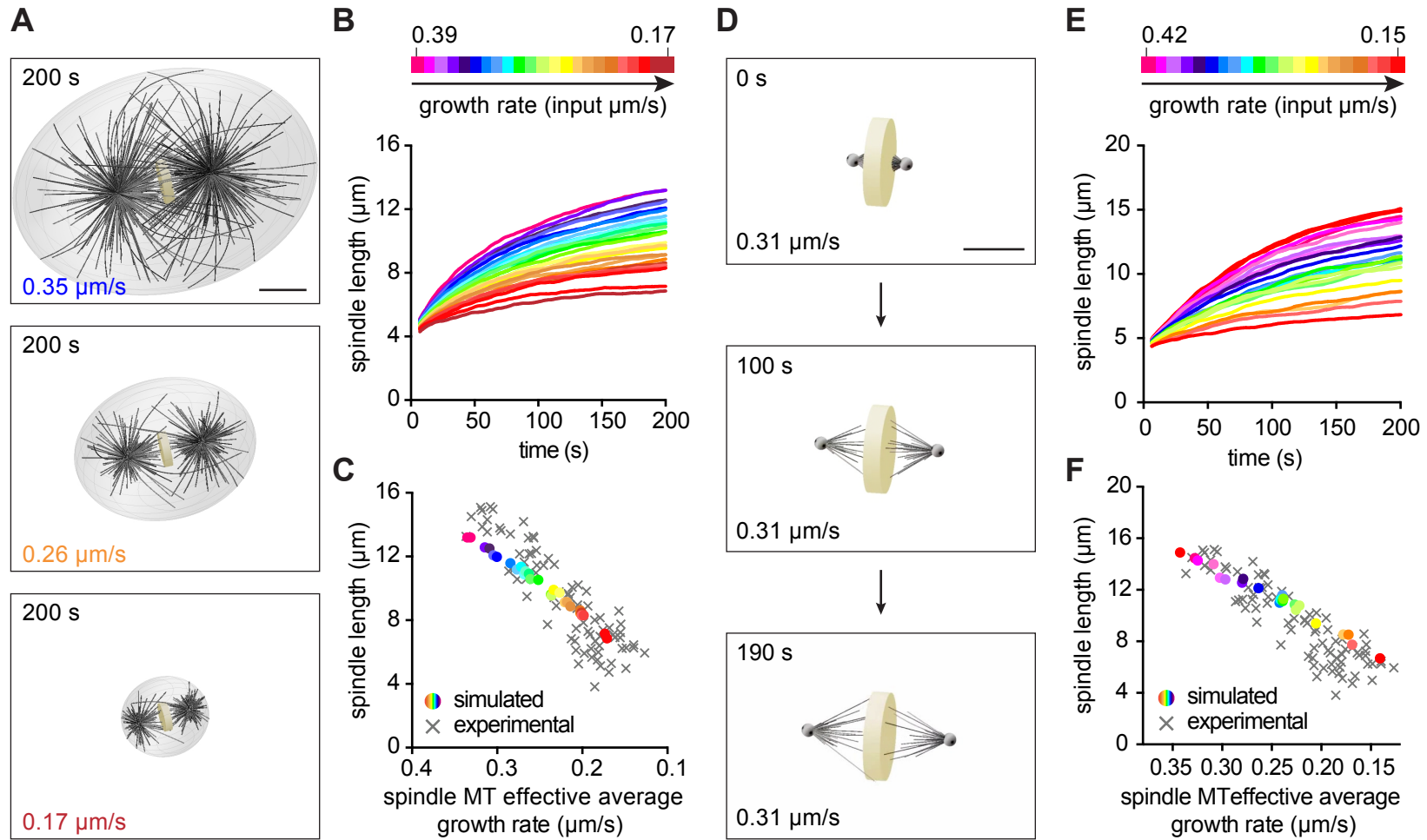


Figure 6

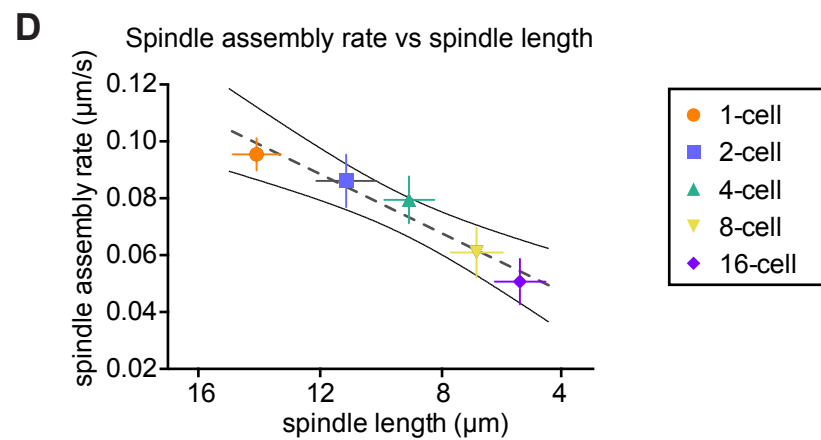
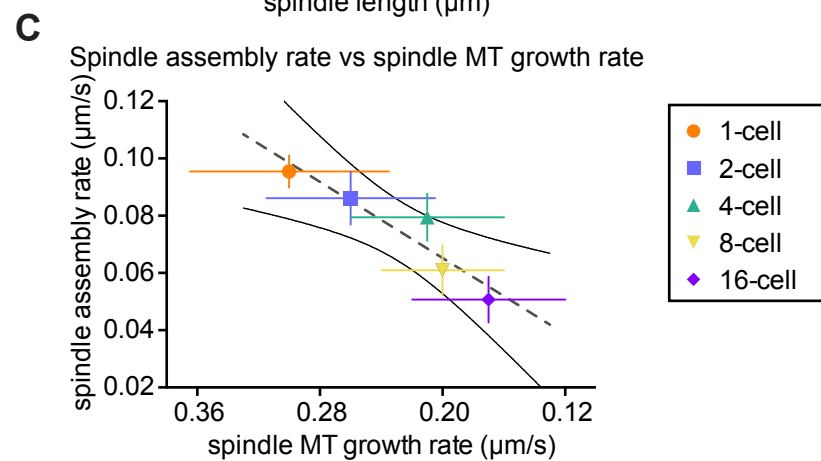
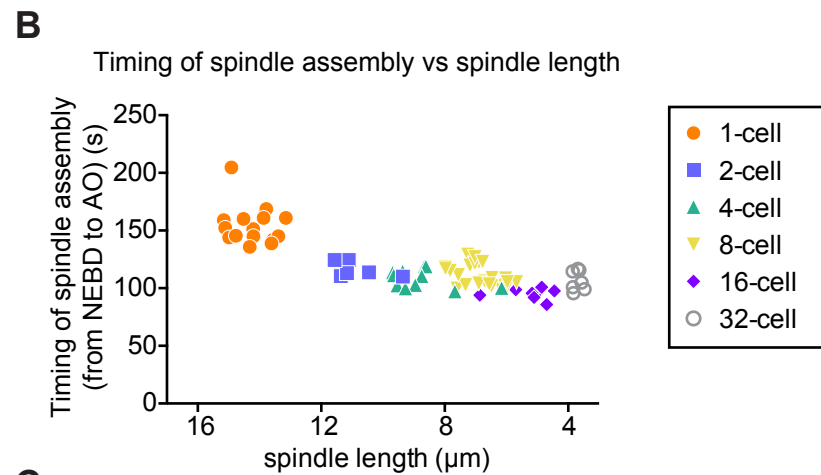
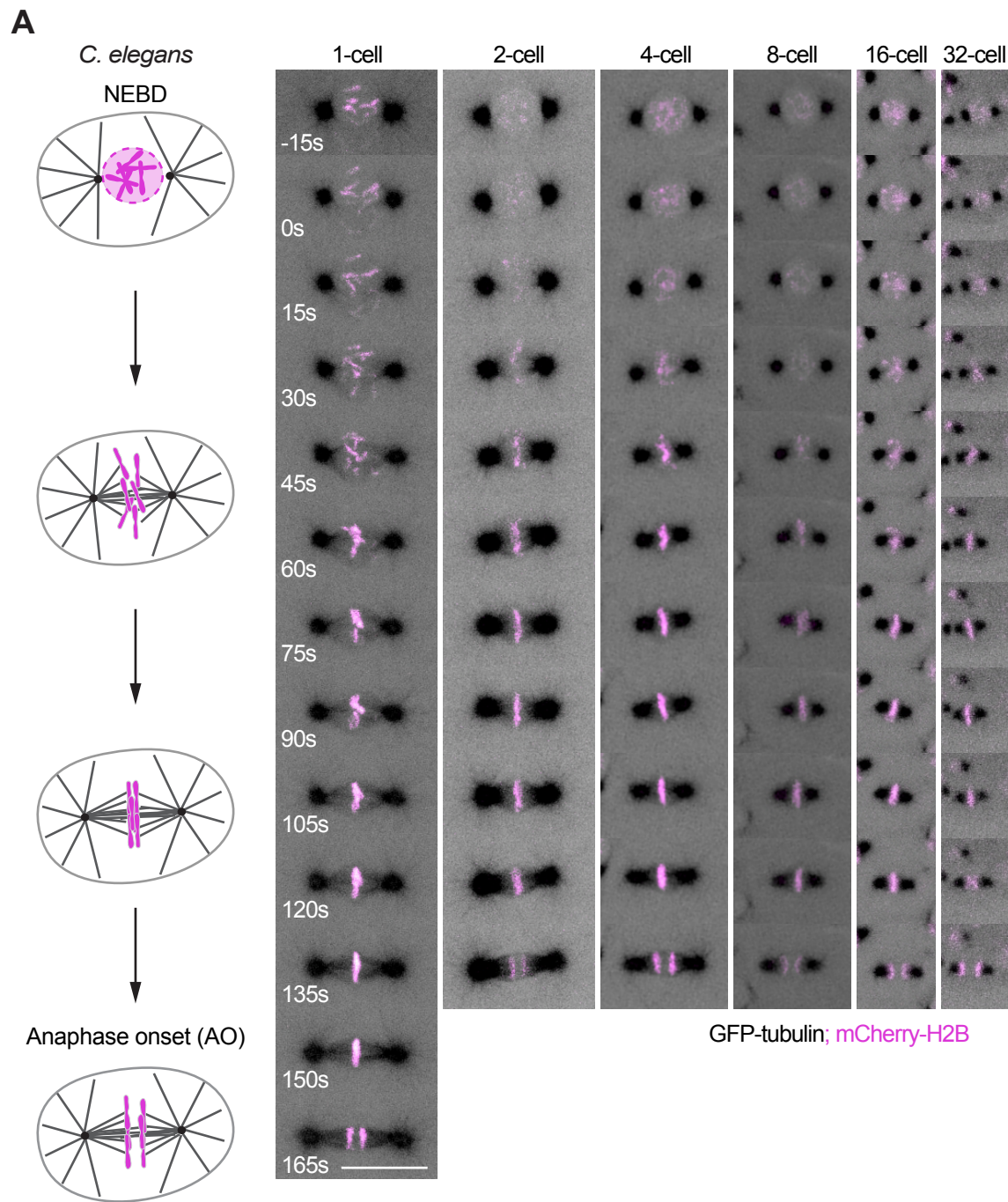
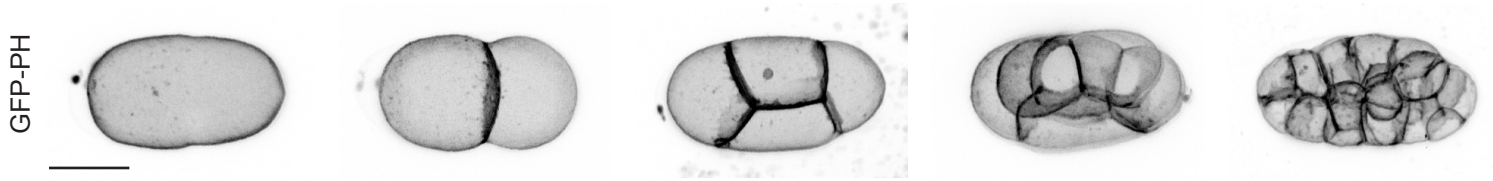
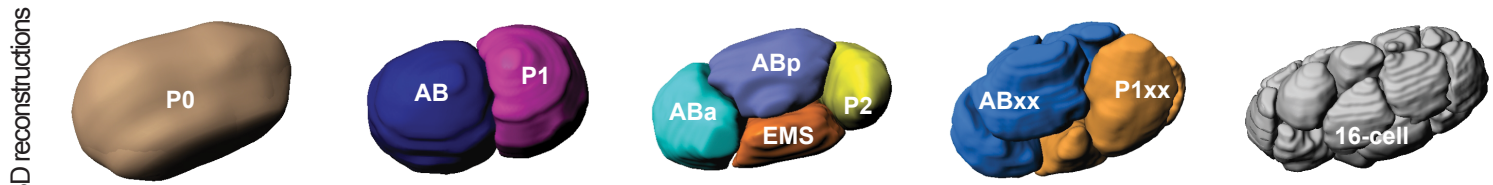


Figure S1

A

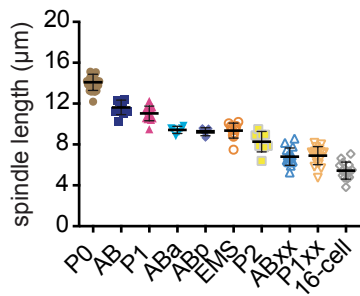


B



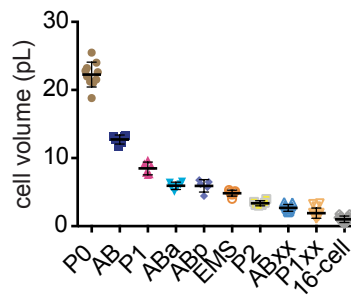
C

Spindle length vs cell type



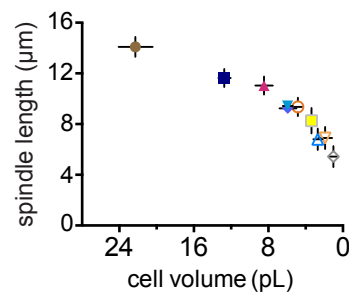
D

Cell volume vs cell type



E

Spindle length vs cell volume



F

Spindle length vs cell volume

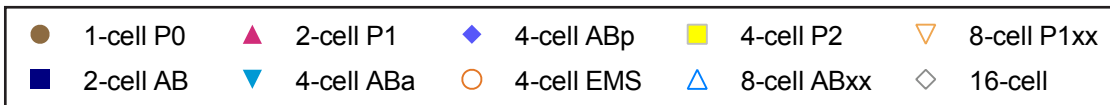
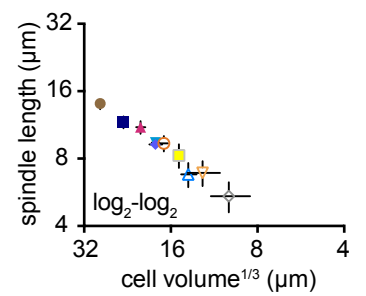


Figure S2

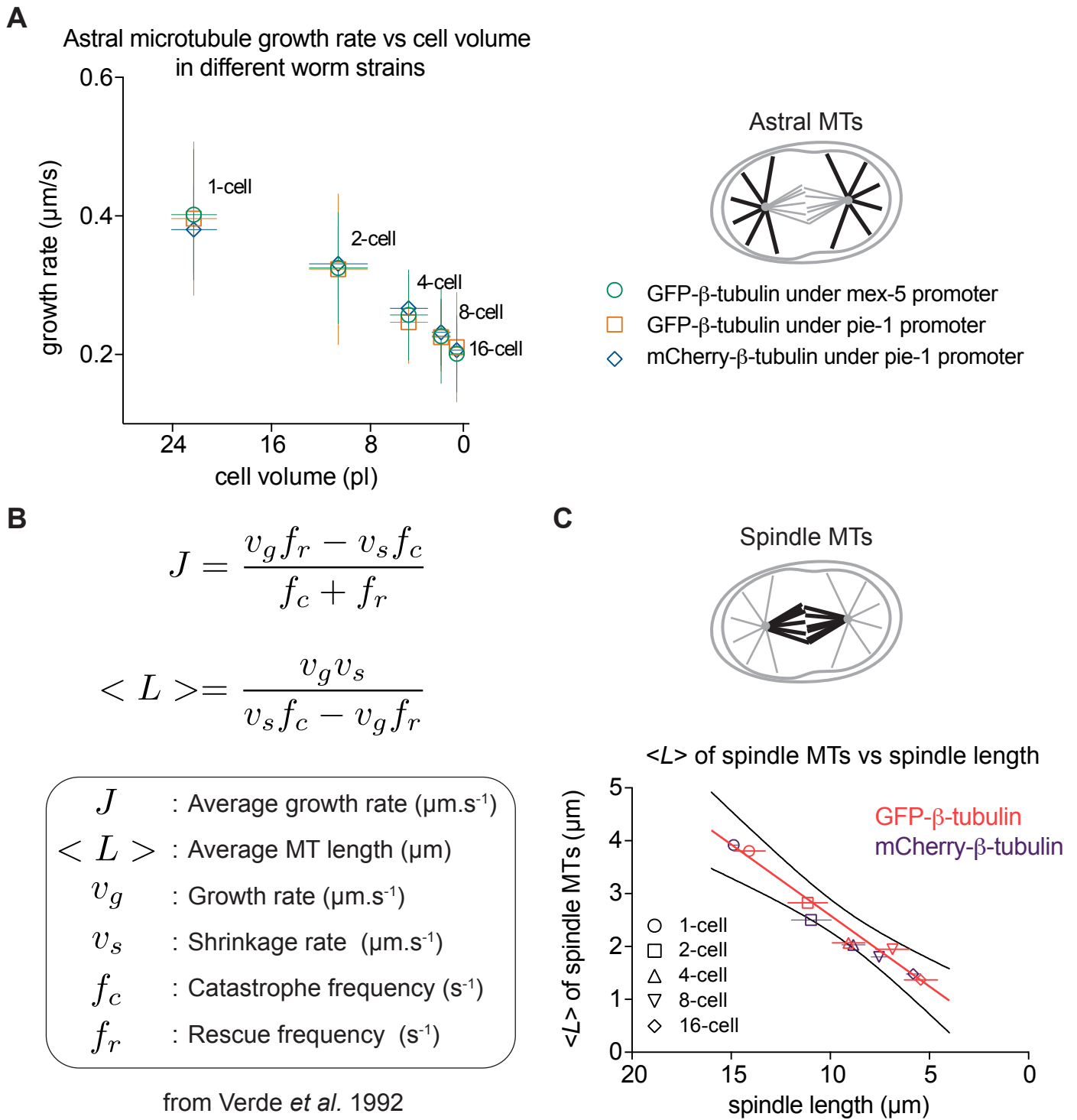


Figure S3

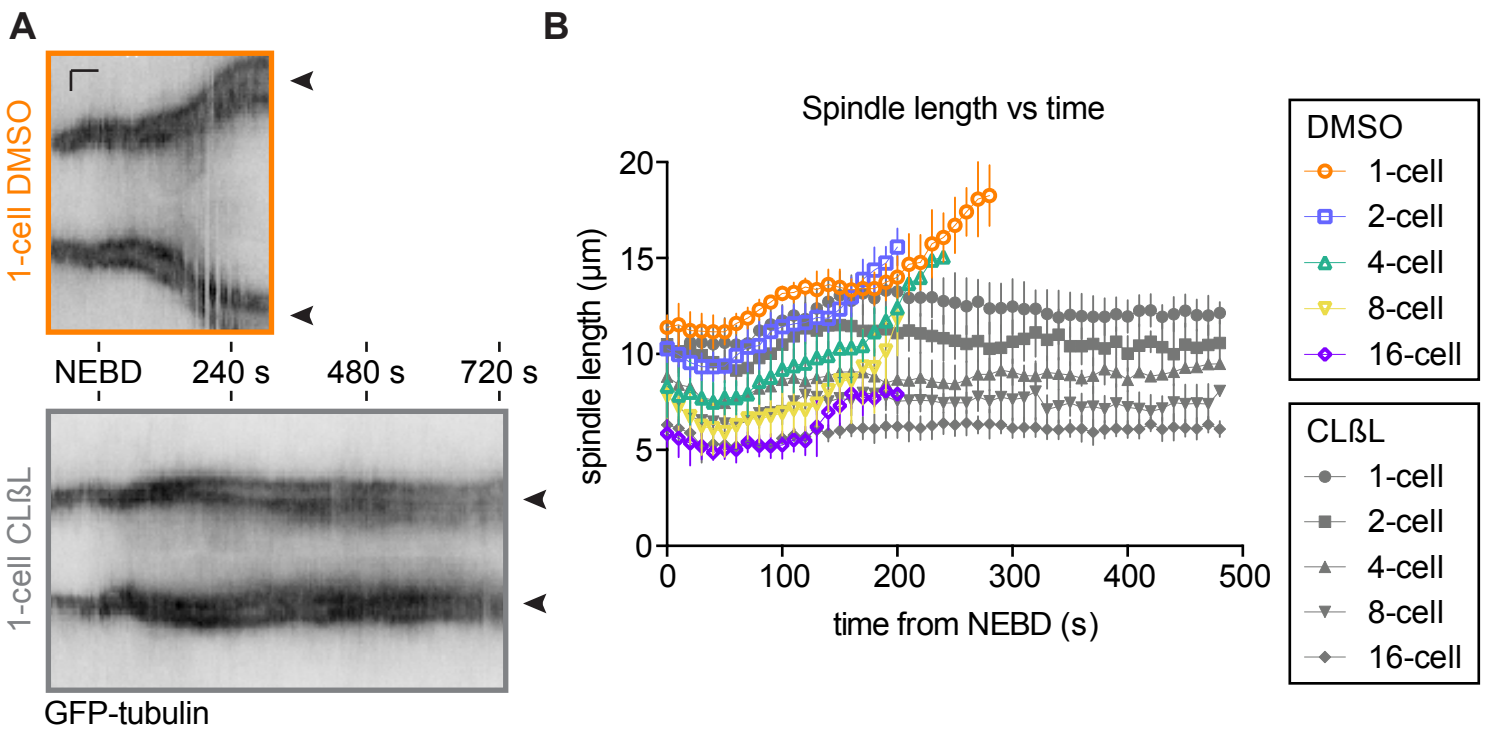
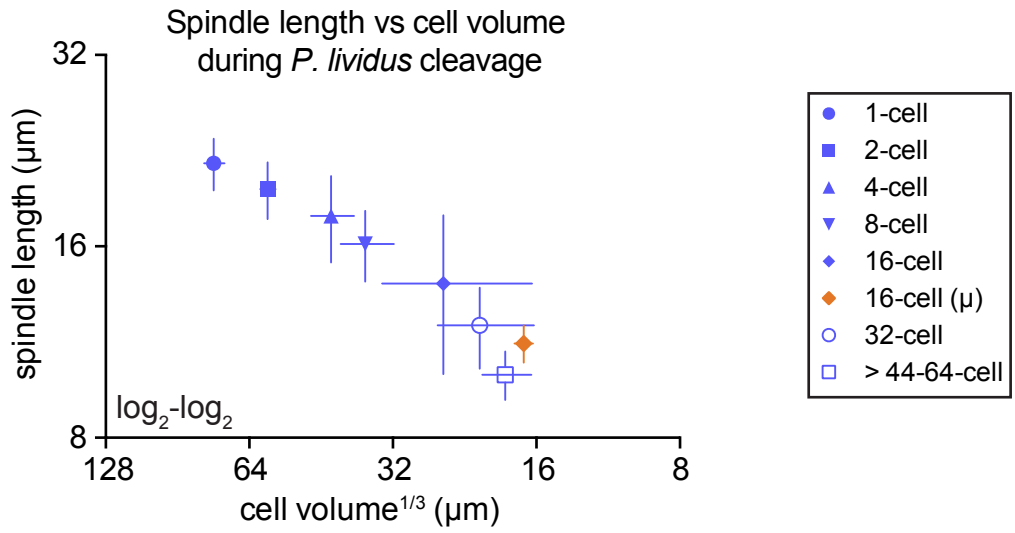


Figure S4

A



B

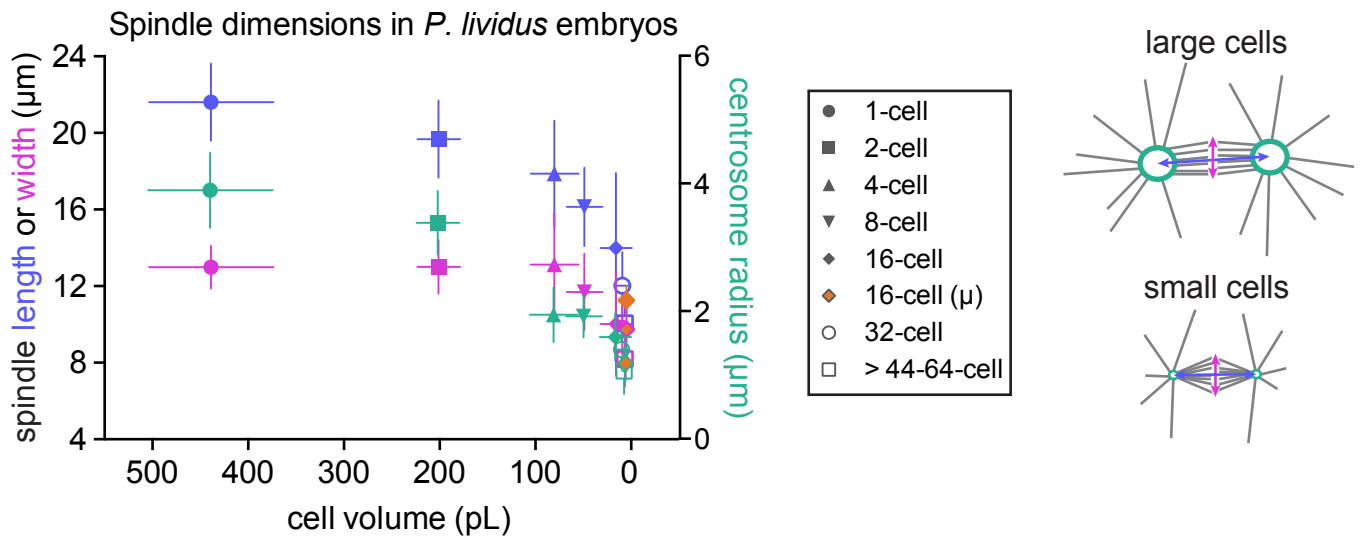


Figure S5

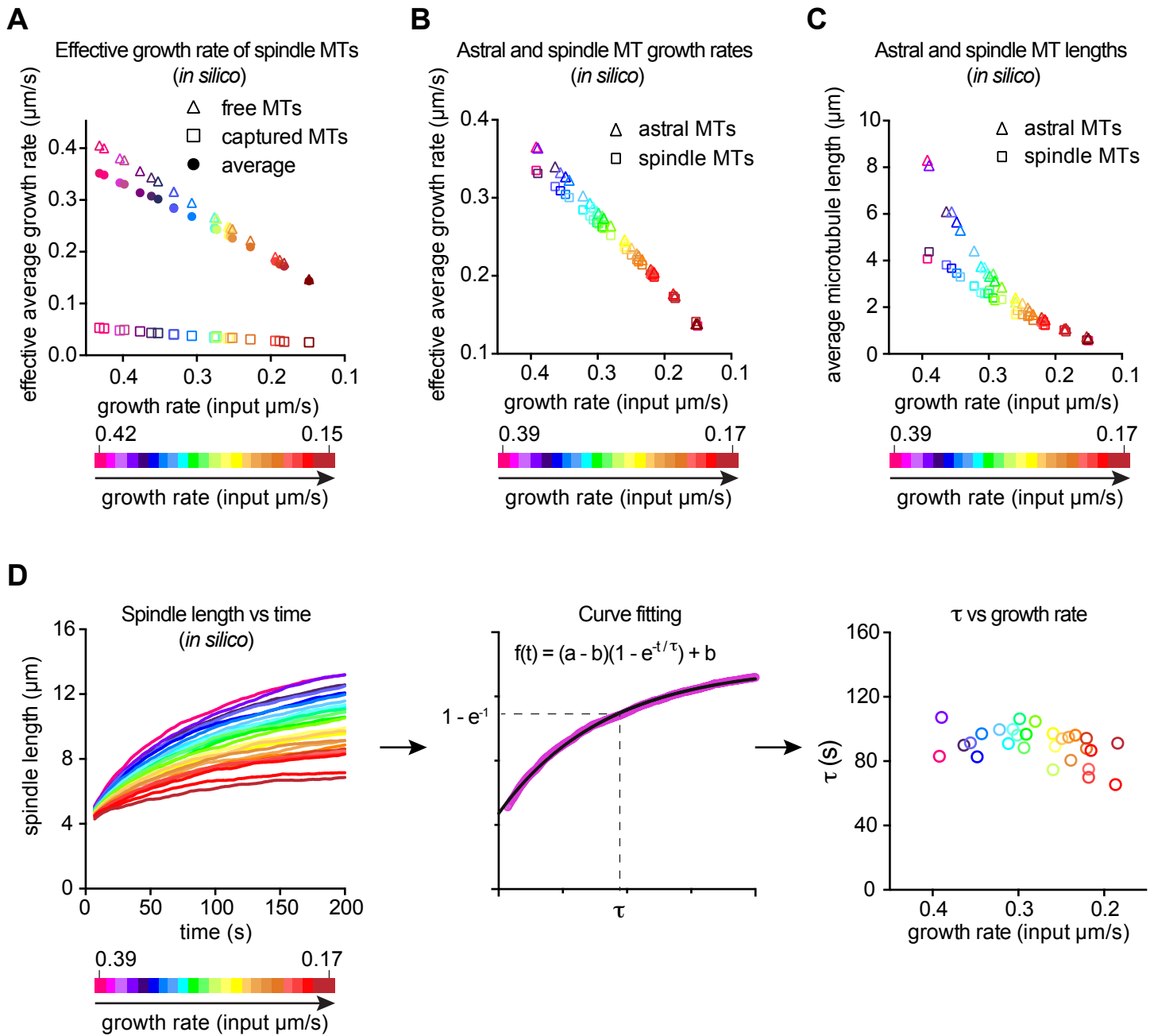
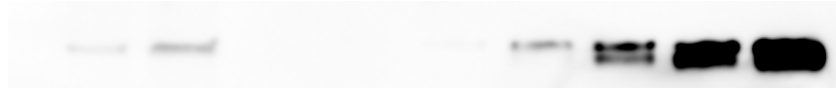


Figure S6

A

nb of embryos		ng of tubulin						
1120	2240	7.8	15.6	31.2	62.5	125	250	500



B

embryo volume = $2.2 \cdot 10^{-11}$ L (Figure 2 and S1)

tubulin concentration in embryo = 18.6 to 24.8 μ M (~22 μ M)

Figure S7

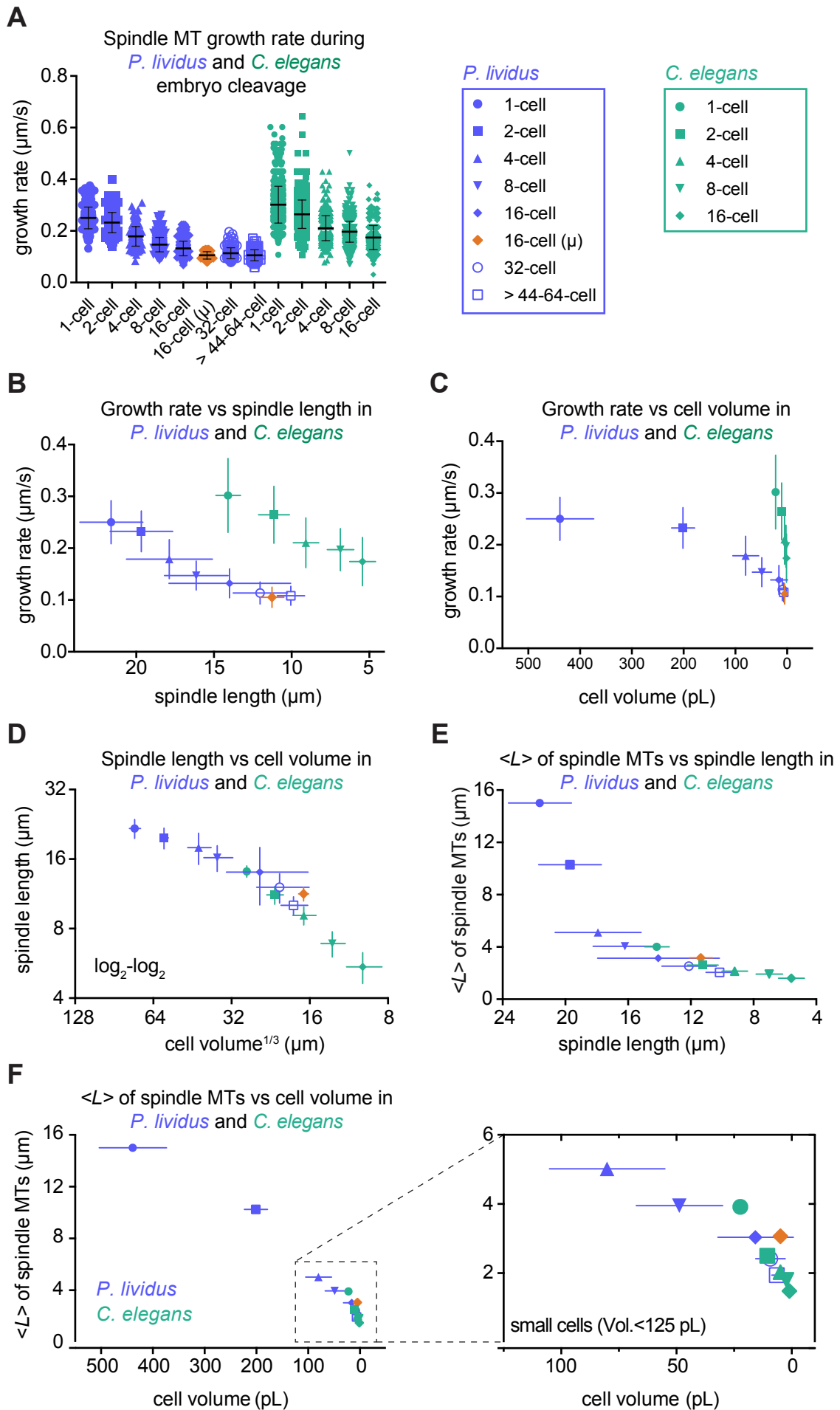


Table S1. Microtubule Dynamics Parameters in *C. elegans* Embryos. Related to Figure 1 to 3 and Figure S2

A

Astral microtubules dynamics in control and RNAi-treated embryos

Control		Growth rate ($\mu\text{m/s}$)			Shrinkage rate ($\mu\text{m/s}$)			Catastrophe freq. (s^{-1})			Rescue freq. (s^{-1})			Cell volume (pL)			Spindle length (μm)			<i>J</i>	<L>
stage	cell	mean	SD	n	mean	SD	n	mean	SD	n	mean	SD	n	mean	SD	n	mean	SD	n	($\mu\text{m/s}$)	(μm)
1-cell	P0	0.4	0.09	2080	0.71	0.38	1129	0.19	0.07	2080	0.32	0.14	1129	22.27	1.83	10	14.09	0.79	24	-0.01	31.55
2-cell	All	0.32	0.08	1320	0.62	0.23	904	0.24	0.07	1320	0.39	0.14	904	10.6	2.35	12	11.14	0.99	23	-0.03	10.58
2-cell	AB	0.32	0.08	610	0.63	0.27	411	0.22	0.06	610	0.38	0.14	411	12.73	0.66	6	11.28	1.29	10	-0.02	10.94
2-cell	P1	0.32	0.08	791	0.61	0.23	545	0.24	0.07	791	0.41	0.14	545	8.48	0.93	6	11.04	0.72	13	-0.02	10.41
4-cell	All	0.26	0.07	2443	0.67	0.26	1630	0.24	0.08	2443	0.43	0.21	1630	4.9	1.52	23	9.08	0.82	33	-0.07	3.47
4-cell	Aba	0.26	0.06	330	0.64	0.22	178	0.25	0.08	330	0.49	0.18	178	5.93	0.54	6	9.42	0.36	6	-0.04	4.64
4-cell	Abp	0.25	0.07	385	0.67	0.24	227	0.23	0.07	385	0.44	0.23	227	5.97	1.04	5	9.25	0.39	7	-0.05	4.04
4-cell	EMS	0.26	0.07	975	0.7	0.28	634	0.25	0.1	975	0.51	0.2	634	4.84	0.44	7	9.35	0.46	12	-0.04	4.74
4-cell	P2	0.25	0.06	754	0.68	0.34	596	0.23	0.09	754	0.37	0.19	596	3.37	0.38	6	8.27	1.00	7	-0.07	2.63
8-cell	All	0.23	0.07	1647	0.57	0.22	1103	0.29	0.10	1647	0.47	0.18	1103	2.29	0.74	27	6.86	0.85	34	-0.07	2.31
8-cell	Abxx	0.23	0.07	1367	0.56	0.23	892	0.3	0.1	1367	0.48	0.19	892	2.69	0.5	13	6.81	0.85	16	-0.07	2.08
8-cell	P1xx	0.22	0.06	653	0.57	0.25	469	0.27	0.09	653	0.47	0.17	469	1.91	0.74	14	6.91	0.88	18	-0.06	2.4
16-cell	16-cell	0.2	0.05	639	0.51	0.21	413	0.32	0.11	639	0.45	0.18	413	1.02	0.48	18	5.44	0.84	15	-0.09	1.4
<i>cls-2^{CLASP}(RNAi)</i>		mean	SD	n	mean	SD	n	mean	SD	n	mean	SD	n	mean	SD	n	mean	SD	n	($\mu\text{m/s}$)	(μm)
1-cell	P0	0.3	0.06	321	0.6	0.18	272	0.23	0.06	321	0.35	0.14	272	-	-	-	8.97	0.94	8	-0.04	5.40
<i>C27D9.1(RNAi)</i>		mean	SD	n	mean	SD	n	mean	SD	n	mean	SD	n	mean	SD	n	mean	SD	n	($\mu\text{m/s}$)	(μm)
1-cell	P0	0.41	0.08	740	0.65	0.2	552	0.2	0.06	740	0.3	0.1	552	-	-	-	18.41	1.01	17	-0.008	39.55

Spindle microtubules dynamics in control and RNAi-treated embryos

Control		Growth rate ($\mu\text{m/s}$)			Shrinkage rate ($\mu\text{m/s}$)			Catastrophe freq. (s^{-1})			Rescue freq. (s^{-1})			Cell volume (pL)			Spindle length (μm)			<i>J</i>	<L>
stage	cell	mean	SD	n	mean	SD	n	mean	SD	n	mean	SD	n	mean	SD	n	mean	SD	n	($\mu\text{m/s}$)	(μm)
1-cell	P0	0.3	0.07	1021	0.65	0.26	743	0.28	0.1	1021	0.44	0.18	743	22.27	1.83	10	14.09	0.79	24	-0.05	3.89
2-cell	All	0.26	0.06	1059	0.72	0.34	679	0.36	0.10	1059	0.70	0.29	679	10.6	2.35	12	11.14	0.99	23	-0.07	2.48
2-cell	AB	0.27	0.05	355	0.75	0.36	246	0.34	0.09	355	0.65	0.28	246	12.73	0.66	6	11.28	1.29	10	-0.07	2.63
2-cell	P1	0.26	0.06	704	0.71	0.33	433	0.37	0.1	704	0.72	0.3	433	8.48	0.93	6	11.04	0.72	13	-0.07	2.44
4-cell	All	0.21	0.05	625	0.66	0.30	405	0.34	0.09	625	0.72	0.29	405	4.9	1.52	23	9.08	0.82	33	-0.07	2.01
4-cell	Aba	0.22	0.04	47	0.54	0.17	43	0.31	0.07	47	0.62	0.18	43	5.93	0.54	6	9.42	0.36	6	-0.04	3.98
4-cell	Abp	0.22	0.05	62	0.51	0.13	53	0.32	0.07	62	0.6	0.16	53	5.97	1.04	5	9.25	0.39	7	-0.04	3.42
4-cell	EMS	0.22	0.05	359	0.69	0.31	226	0.34	0.1	359	0.78	0.33	226	4.84	0.44	7	9.35	0.46	12	-0.07	2.12
4-cell	P2	0.2	0.05	173	0.69	0.33	99	0.34	0.08	173	0.73	0.29	99	3.37	0.38	6	8.27	1.00	7	-0.09	1.57
8-cell	All	0.20	0.04	909	0.59	0.24	555	0.31	0.11	909	0.60	0.26	555	2.29	0.74	27	6.86	0.85	34	-0.07	1.78
8-cell	Abxx	0.2	0.04	247	0.54	0.21	173	0.28	0.09	247	0.52	0.19	173	2.69	0.5	13	6.81	0.85	16	-0.06	2
8-cell	P1xx	0.2	0.04	662	0.61	0.25	382	0.32	0.12	662	0.64	0.29	382	1.91	0.74	14	6.91	0.88	18	-0.07	1.74
16-cell	16-cell	0.17	0.05	422	0.65	0.31	288	0.33	0.1	422	0.77	0.29	288	1.02	0.48	18	5.44	0.84	15	-0.08	1.46
<i>cls-2^{CLASP}(RNAi)</i>		mean	SD	n	mean	SD	n	mean	SD	n	mean	SD	n	mean	SD	n	mean	SD	n	($\mu\text{m/s}$)	(μm)
1-cell	P0	0.25	0.06	556	0.63	0.20	458	0.33	0.12	556	0.52	0.22	458	-	-	-	8.97	0.94	8	-0.08	2.02
<i>C27D9.1(RNAi)</i>		mean	SD	n	mean	SD	n	mean	SD	n	mean	SD	n	mean	SD	n	mean	SD	n	($\mu\text{m/s}$)	(μm)
1-cell	P0	0.38	0.08	772	0.65	0.16	758	0.27	0.07	772	0.35	0.03	758	-	-	-	18.41	1.01	17	-0.07	5.78

B

Astral microtubule growth rate in different *C. elegans* strains

	mex-5p>GFP- β -tubulin			pie-1p>GFP- β -tubulin			pie-1p>mCherry- β -tubulin		
	mean	SD	n	mean	SD	n	mean	SD	n
1-cell	0.40	0.09	2080	0.40	0.11	295	0.38	0.06	321
2-cell	0.32	0.08	1320	0.32	0.11	188	0.33	0.05	333
4-cell	0.26	0.07	2443	0.25	0.06	234	0.27	0.05	442
8-cell	0.23	0.07	1647	0.23	0.05	197	0.23	0.05	378
16-cell	0.20	0.05	639	0.21	0.08	114	0.21	0.04	295

C

Spindle microtubule dynamics in different *C. elegans* strains

	Growth rate ($\mu\text{m/s}$)			Shrinkage rate ($\mu\text{m/s}$)			Catastrophe frequency (s^{-1})			Rescue frequency (s^{-1})			<i>J</i>	<L>	
	mean	SD	n	mean	SD	n	mean	SD	n	mean	SD	n	$\mu\text{m/s}$	μm	
mex-5p>GFP-β-tubulin															
1 cell	0.30	0.07	1021	0.65	0.26	743	0.28	0.10	1021	0.44	0.18	743	-0.05	3.89	
2 cells	0.26	0.06	1059	0.72	0.34	679	0.36	0.10	1021	0.70	0.29	679	-0.07	2.48	
4 cells	0.21	0.05	625	0.66	0.30	405	0.34	0.09	625	0.72	0.29	405	-0.07	2.01	
8 cells	0.20	0.04	909	0.59	0.24	555	0.31	0.11	909	0.60	0.26	555	-0.07	1.78	
16 cells	0.17	0.05	422	0.65	0.31	288	0.33	0.10	422	0.77	0.29	288	-0.08	1.46	
pie-1p>mCherry-β-tubulin															
1 cell	0.29	0.04	171	0.65	0.15	183	0.25	0.04	171	0.40	0.09	183	-0.05	3.78	
2 cells	0.26	0.04	149	0.66	0.18	119	0.32	0.09	149	0.58	0.22	119	-0.06	2.80	
4 cells	0.22	0.04	194	0.66	0.19	144	0.35	0.08	194	0.73	0.25	144	-0.07	2.04	
8 cells	0.20	0.04	213	0.62	0.18	123	0.32	0.08	213	0.68	0.21	123	-0.07	1.92	
16 cells	0.18	0.03	278	0.60	0.18	266	0.32	0.06	278	0.63	0.17	266	-0.09	1.35	

Table S2. Microtubule Dynamics, Spindle and Cell Dimensions in *Caenorhabditis elegans* and *Paracentrotus lividus*. Related to Figure 4, S4 and S6

A

***C. elegans* and *P. lividus* spindle microtubules dynamics parameters. spindle length and cell volume**

<i>C. elegans</i>																				
Growth rate (μm/s)			Shrinkage rate (μm/s)			Catastrophe freq. (s ⁻¹)			Rescue freq. (s ⁻¹)			Spindle length (μm)			Cell volume (pL)			<i>J</i>	<L>	
stage	mean	SD	N	mean	SD	N	mean	SD	N	mean	SD	N	mean	SD	N	mean	SD	N	(μm/s)	(μm)
1-cell	0.30	0.07	1021	0.65	0.26	743	0.28	0.10	1021	0.44	0.18	743	14.09	0.79	24	22.27	1.83	10	-0.07	3.89
2-cell	0.26	0.06	1059	0.72	0.34	679	0.36	0.10	1059	0.70	0.29	679	11.14	0.99	23	10.6	2.35	12	-0.07	2.48
4-cell	0.21	0.05	625	0.66	0.30	405	0.34	0.09	625	0.72	0.29	405	9.08	0.82	33	4.9	1.52	23	-0.07	2.01
8-cell	0.20	0.04	909	0.59	0.24	555	0.31	0.11	909	0.60	0.26	555	6.86	0.85	34	2.29	0.74	27	-0.07	1.78
16-cell	0.17	0.05	422	0.65	0.31	288	0.33	0.10	422	0.77	0.29	288	5.44	0.84	15	1.02	0.48	18	-0.07	1.46
<i>P. lividus</i>																				
Growth rate (μm/s)			Shrinkage rate (μm/s)			Catastrophe freq. (s ⁻¹)			Rescue freq. (s ⁻¹)			Spindle length (μm)			Cell volume (pL)			<i>J</i>	<L>	
stage	mean	SD	N	mean	SD	N	mean	SD	N	mean	SD	N	mean	SD	N	mean	SD	N	(μm/s)	(μm)
1-cell	0.25	0.04	276	0.47	0.19	104	0.14	0.04	276	0.23	0.07	104	21.61	2.02	13	438.81	65.0	13	-0.01	15.01
2-cell	0.23	0.04	391	0.42	0.18	189	0.14	0.04	391	0.22	0.08	189	19.68	2.02	9	201.19	22.38	9	-0.02	10.24
4-cell	0.18	0.04	187	0.37	0.09	103	0.15	0.04	187	0.24	0.07	103	17.87	2.77	7	80.1	25.05	7	-0.03	5.02
8-cell	0.15	0.03	500	0.36	0.11	276	0.13	0.03	500	0.23	0.06	276	16.14	2.05	17	48.77	18.73	17	-0.03	3.95
16-cell	0.13	0.03	341	0.37	0.12	189	0.13	0.03	341	0.24	0.08	189	13.99	3.92	7	15.74	16.39	7	-0.03	3.04
16-cell μ	0.11	0.01	92	0.35	0.07	72	0.12	0.03	92	0.26	0.06	72	11.26	0.76	5	4.91	0.66	5	-0.03	2.3
32-cell	0.11	0.02	150	0.38	0.15	55	0.12	0.03	150	0.26	0.09	55	12.03	1.75	9	9.28	6.38	9	-0.04	2.42
44-64-cell	0.11	0.02	97	0.35	0.11	58	0.15	0.04	97	0.28	0.09	58	10.05	0.88	5	6.43	2.29	5	-0.04	1.98

B

***C. elegans* and *P. lividus* cell and spindle dimensions**

<i>C. elegans</i>																			
Spindle length (μm)			Spindle width (μm)			Metaphase plate thickness(μm)			Centrosome radius (μm)			Cell perimeter (μm)			Cell volume (pL)				
stage	mean	SD	N	mean	SD	N	mean	SD	N	mean	SD	N	mean	SD	N	mean	error	N	
1-cell	14.09	0.79	24	5.96	0.84	24	1.3	0.33	34	0.76	0.14	35	135.73	6.81	24	22.27	1.83	10	
2-cell	11.14	0.99	23	5.35	0.47	23	1.09	0.24	56	0.59	0.13	63	94.62	9.2	27	10.6	2.35	12	
4-cell	9.08	0.82	33	5.64	2.83	33	1.03	0.21	25	0.48	0.08	37	68.89	7.33	43	4.9	1.52	23	
8-cell	6.86	0.85	34	3.99	0.47	34	1.19	0.36	51	0.44	0.08	47	48.69	5.7	39	2.29	0.74	27	
16-cell	5.44	0.84	15	3.21	0.42	15	0.81	0.13	24	0.35	0.06	36	34.26	5.74	19	1.02	0.48	18	
<i>P. lividus</i>																			
Spindle length (μm)			Spindle width (μm)			Metaphase plate thickness(μm)			Centrosome radius (μm)			Cell perimeter (μm)			Cell volume (pL)				
stage	mean	SD	N	mean	SD	N	mean	SD	N	mean	SD	N	mean	SD	N	mean	error	N	
1-cell	21.61	2.02	13	12.99	1.11	13	-	-	-	3.9	0.59	26	296.19	14.62	13	438.81	65.0	13	
2-cell	19.68	2.02	9	13.01	1.4	9	-	-	-	3.39	0.5	18	228.39	8.47	9	201.19	22.38	9	
4-cell	17.87	2.77	7	13.13	2.7	7	-	-	-	1.95	0.43	14	168.02	17.51	7	80.1	25.05	7	
8-cell	16.14	2.05	17	11.69	2	17	-	-	-	1.93	0.33	34	142.41	18.23	17	48.77	18.73	17	
16-cell	13.99	3.92	7	10.03	2.68	7	-	-	-	1.6	0.37	14	97.67	33.92	7	15.74	16.39	7	
16-cell μ	11.26	0.76	5	9.74	1.62	5	-	-	-	1.19	0.27	12	66.26	2.96	5	4.91	0.66	5	
32-cell	12.03	1.75	9	9.77	1.39	9	-	-	-	1.41	0.31	18	81.91	18.75	9	9.28	6.38	9	
44-64-cell	10.05	0.88	5	8.19	1.45	5	-	-	-	1.07	0.36	10	72.49	8.59	5	6.43	2.29	5	

Table S3. Parameters used in the simulations. Related to Figure 5 and S5.

Parameter		Description/reference
<u>Microtubules (MTs)</u>		
Rigidity	30 pN.μm ²	Corresponds to a persistence length of 7 mm (Gittes et al., 1993)
Growth rate (input)	$V_0 = 0.14$ to 0.43 μm/s	Varied in each simulation between 0.14 and 0.43 μm/s (range of experimental growth rate observed in <i>C. elegans</i> in this study)
Effective growth rate	$V_g = V_0 \cdot \exp(-F/F_{stall})$	Under antagonistic force (F) growth rate was reduced (Dogterom and Yurke 1997)
Stall force	$F_{stall} = 5$ pN	From Dogterom and Yurke, 1997
Shrinkage rate	0.65 μm/s	This study (average shrinkage rate of spindle MTs from 1- to 16-cell stage in <i>C. elegans</i>)
Rescue frequency	0.5 s ⁻¹	This study (average rescue frequency of spindle MTs from 1- to 16-cell stage in <i>C. elegans</i>)
Catastrophe frequency (fc)	$fc_0 = 0.3$; $fc_{stall} = 0.6$ s ⁻¹	fc_0 corresponds to the average catastrophe frequency of freely growing MTs (measured in this study). The catastrophe frequency of stalled MTs (fc_{stall}) was estimated doubled compare to free MTs ($2 \cdot fc_0$). In Cytosim catastrophe frequency can be increased with opposing force as described by Janson et al., 2003. Force induced catastrophe was only considered in simulations using astral MTs confined in space (Figure 5A-C) Catastrophe frequency is expressed in Cytosim as: $fc = fc_{stall} / (1 + (fc_{stall}/fc_0 - 1)V_g/V_0)$
<u>MT nucleation</u>		
		MTs were only nucleated at centrosomes, the number of MTs per aster was constant
<u>Centrosomes</u>		
Viscosity	200 pN.s/μm ²	From Letort et al., 2016. In Cytosim the mobility of the bead used to mimic centrosome is dependent on its effective viscosity (200 pN.s/μm ²). This does not influence MTs mobility
Radius	0.5 μm	Average radius measured in this study
Fibers	50 or 500 MTs per aster	50 MTs when only spindle MTs were simulated. 500 MTs including 100 constrained spindle MTs when astral were simulated
Spindle angle	0.6 rad	Constrains spindle MTs into a right circular cone with a semi-angle of ~30°. This angle was estimated from our measurements of spindle geometry (Table S2)
<u>Metaphase plate</u>		
Shape and dimensions	Solid cylinder	Cylinder dimensions varied in each simulation and were extrapolated from experimental data (Table S2). MTs were confined outside the plate
Couple		Couples are made of two singles called « hands » and link MTs to metaphase plate
Hand1	Hands binding to plate	Anchored to the metaphase plate. Avoid MT sliding away when attached to the plate
Hand2	Hands binding to MTs	Bind only free growing MTs with very high binding rate
<u>Confinement space</u>		
Cell space	unconfined or 3D ellipse	Dimensions of the ellipse were extrapolated from <i>C.elegans</i> embryo dimensions. In simulations with astral MTs, all objects were confined within the ellipse (Figure 5A-C).
<u>Simulation parameters</u>		
Time step	0.05 s	Nédélec et al., 2007
kT	0.0042 pN.μm	Corresponds to a temperature of 25°C
Viscosity	1 pN.s/μm ²	Cytoplasmic viscosity. Kole et al., 2005; Nedelec and Foethke, 2007; Letort et al., 2016